Combined forces of hydrostatic pressure and actin polymerization drive endothelial tip cell migration and sprouting angiogenesis

Igor Kondrychyn[1], Haymar Wint[1], Liqun He[2], Christer Betsholtz[2, 3] and Li-Kun Phng[1*]

[1] Laboratory for Vascular Morphogenesis, RIKEN Center for Biosystems Dynamics Research, Kobe 650-0047, Japan

[2] Department of Immunology, Genetics and Pathology, Rudbeck Laboratory, Uppsala University, 75185 Uppsala, Sweden

[3] Department of Medicine Huddinge, Karolinska Institutet, 14157 Huddinge, Sweden

* Correspondence: likun.phng@riken.jp

SUMMARY

Cell migration is a key process in the shaping and formation of tissues. During sprouting angiogenesis, endothelial tip cells invade avascular tissues by generating actomyosin-dependent forces that drive cell migration and vascular expansion. Surprisingly, ECs can still invade if actin polymerization is inhibited. In this study, we show that endothelial tip cells employ an alternative mechanism of cell migration that is dependent on Aquaporin (Aqp)-mediated water inflow and increase in hydrostatic pressure. In the zebrafish, ECs express *aqp1a.1* and *aqp8a.1* in newly formed vascular sprouts in a VEGFR2-dependent manner. Aqp1a.1 and Aqp8a.1 loss-of-function studies show an impairment in intersegmental vessels formation because of a decreased capacity of tip cells to increase their cytoplasmic volume and generate membrane protrusions, leading to delayed tip cell emergence from the dorsal aorta and slower migration. Further inhibition of actin polymerization resulted in a greater decrease in sprouting angiogenesis, indicating that ECs employ two mechanisms for robust cell migration *in vivo*. Our study highlights an important role of hydrostatic pressure in tissue morphogenesis.

Keywords

Endothelial cell migration, Sprouting angiogenesis, Aquaporin, Water flow, Hydostatic Pressure, Actin, Zebrafish

INTRODUCTION

The blood vascular system is a dynamic, multicellular tissue that adapts to the metabolic demands of development, growth and homeostasis by altering its pattern and morphology. Macroscopic transformation in the vascular network is achieved by microscopic changes in endothelial cell (EC) behaviours. For example, vascular expansion through sprouting angiogenesis requires the coordination of EC migration, proliferation, anastomosis, lumen formation and cell rearrangements, all of which require specific cell shape changes. At the initial phase of sprouting angiogenesis, endothelial tip cells generate numerous membrane protrusions such as filopodia and lamellipodia that drive migration and anastomosis (Figueiredo et al., 2021; Gerhardt et al., 2003; Phng et al., 2013; Sauteur et al., 2017). During tubulogenesis, apical membranes deform by generating inverse blebs to expand lumens so that blood can be transported efficiently through the blood vascular network (Gebala et al., 2016). However, following vessel perfusion, ECs become less dynamic and instead develop resistance to the deforming forces of blood pressure to maintain vessel morphology (Kondrychyn et al., 2020). EC shape is therefore dynamic and changes depending on the morphogenetic state of vascular development.

It is well established that localized remodelling of actin cytoskeleton and non-myosin II contractility are instrumental in driving cell shape changes during tissue morphogenesis (Clarke and Martin, 2021; Munjal and Lecuit, 2014; Murrell et al., 2015). More recently, there is an accumulating body of work implicating a role of water flow and the resulting changes in hydrostatic pressure as another mechanical mechanism of cell shape change (Choudhury et al., 2022; Chugh et al., 2022; Li et al., 2020). For example, in the osmotic engine model of cell migration, water inflow at the leading edge and outflow at the rear leads to forward translocation of tumour cells in confined microenvironment (Stroka et al., 2014). Additionally, hydrostatic pressure from the extracellular environment can drive tissue morphogenesis, as demonstrated during mouse blastocyst formation (Chan et al., 2019; Dumortier et al., 2019), development of the otic vesicle in the zebrafish (Mosaliganti et al., 2019) and blood vessel lumen expansion (Gebala et al., 2016). Hydrostatic pressure can therefore generate sufficient forces to shape tissues and organs to their proper form and size during development.

We have previously discovered that EC migration persists after the inhibition of actin polymerization and in the absence of filopodia to generate new blood vessels in the zebrafish (Phng et al., 2013). This observation suggests the existence of an alternative mechanism of migration

independent of actin polymerization. In this study, we sought to determine whether hydrostatic pressure regulates EC migration during sprouting angiogenesis in the zebrafish by investigating the function of Aquaporins (Aqp), which are transmembrane water channels that increase water permeability of cell membranes to promote transcellular water flow (Day et al., 2014; Farinas et al., 1997; Kozono et al., 2002; Preston et al., 1992). We discovered that ECs of newly formed intersegmental vessels (ISV) express *aqp1a.1* and *aqp8a.1* mRNA, and observed the enrichment of Aqp1a.1 and Aqp8a.1 proteins in the leading edge of migrating tip cells. Detailed single cell analyses showed that endothelial tip cells lacking *aqp1a.1* and *aqp8a.1* expression have reduced cell volume, membrane protrusions and migration capacity. As a result, there is defective sprouting angiogenesis and ISV formation in *aqp1a.1;aqp8a.1* double mutant zebrafish. Notably, when actin polymerization is inhibited in *aqp1a.1*;*aqp8a.1* double mutant zebrafish, there is a greater impairment in EC migration and sprouting angiogenesis, demonstrating the additive function of actin polymerization and hydrostatic pressure (that is created by water inflow) in generating membrane protrusions to drive EC migration *in vivo*.

RESULTS

aqp1a.1 and *aqp8a.1* are differentially expressed by tip and stalk cells during sprouting angiogenesis

Of the 18 number of *aquaporin* genes that are expressed in zebrafish (Tingaud-Sequeira et al., 2010), *aqp1a.1* and *aqp8a.1* mRNA have been detected in blood endothelial cells (ECs) (Koun et al., 2016; Rehn et al., 2011). We confirmed the endothelial expression of *aqp1a.1* and *aqp8a.1* at 30 hours post fertilization (hpf) and 2-, 3- and 4-days post fertilization (dpf) by whole-mount *in situ* hybridization (Fig. S1). The two endothelial *aqp* genes, however, differ in spatial expression. While *aqp1a.1* is widely expressed in blood vessels of the head and trunk (dorsal aorta (DA), caudal artery (CA), ISVs, dorsal longitudinal anastomotic vessels (DLAV) and caudal vein plexus) at 30 hpf, *aqp8a.1* expression is absent in cerebral blood vessels and is restricted to the DA, CA and the ventral regions of ISVs in the trunk. After 1 dpf, *aqp8a.1* expression expands to the entire ISV and DLAV. Additionally, the expression of *aqp1a.1* and *aqp8a.1* gradually decreases in the DA and CA so that both are absent by 4 dpf. Single cell RNA sequencing (scRNAseq) of ECs isolated at 34 hpf and 3 dpf further confirmed the endothelial expression of *aqp1a.1* and *aqp8a.1*

94 mRNA (Fig. S2 A - D), revealed differential expression of *aqp1a.1* and *aqp8a.1* mRNA in distinct
95 endothelial clusters and highlighted higher *aqp1a.1* transcript expression in all endothelial
96 subtypes compared to *aqp8a.1* (Fig. S2 E - H).
97 We next examined the expression pattern of *aqp1a.1* and *aqp8a.1* at the beginning of
98 sprouting angiogenesis at higher resolution using RNAscope and confocal microscopy. At 20 hpf,
99 *aqp1a.1* mRNA is highly expressed in the DA with little expression in the PCV (Fig. 1A, C and
100 Fig. S3). Closer inspection uncovered heterogeneous expression in the DA, with higher expression
101 in ECs that would be specified as tip cells (Fig. 1A, C and Fig. S3B). Indeed, tip cells of newly
102 formed vascular sprouts express higher levels of *aqp1a.1* compared to adjacent ECs in the DA at
103 20 hpf (Fig. 1A – C, Fig. S3B) and the majority of ISVs (61%) display higher *aqp1a.1* expression
104 in tip cells than in trailing stalk cells at 22 hpf (Fig. 1G). Although we previously observed *aqp8a.1*
105 mRNA in the DA at 30 hpf (Fig. S1), its expression here is largely absent at 20 hpf (Fig. 1B, D
106 and Fig. S3C). At 22hpf, *aqp8a.1* mRNA expression in the DA increases (Fig. 1E and F).
107 Interestingly, unlike *aqp1a.1*, in 78% of ISVs analyzed, *aqp8a.1* mRNA is more highly expressed
108 in stalk cells than tip cells (Fig. 1G). These observations highlight differential expression pattern
109 of *aqp1a.1* and *aqp8a.1* in newly formed vascular sprouts, with *aqp1a.1* expression enriched in tip
110 cells and *aqp8a.1* expression in stalk cells.
111
112 **VEGF-VEGFR2 signalling induces the expression of *aqp1a.1* and *aqp8a.1* mRNA**
113 As *aqp1a.1* and *aqp8a.1* mRNA display differential tip-stalk cell expression, we explored whether
114 their expression is regulated by the VEGFR2-Notch signalling axis, which controls endothelial tip-
115 stalk cell specification during sprouting angiogenesis (Benedito and Hellström, 2013; Phng and
116 Gerhardt, 2009; Siekmann et al., 2013). To inhibit VEGFR2 activity, embryos were treated with 1
117 μM ki8751 from 20 hpf. Relative quantitative polymerase chain reaction (qPCR) experiments
118 showed that *aqp1a.1* mRNA expression was suppressed by 52% after 6 hours ($p < 0.0001$) and
119 by 40% after 24 hours ($p < 0.0001$) of ki8751 treatment when compared to DMSO-treated embryos
120 (Fig. 1H). *aqp8a.1* mRNA expression was also decreased by the inhibition of VEGFR2 activity,
121 and its suppression was accentuated after 24 hours treatment (93% decrease, $p < 0.0001$) compared
122 to after 6 hours (17% decrease, $p = 0.0028$). These results demonstrate that VEGFR2 activity
123 upregulates the expression of *aqp1a.1* and *aqp8a.1*, but the temporal dynamics is different for
124 *aqp1a.1* and *aqp8a.1*. To examine whether VEGFR2 activity also regulates Aquaporin expression

125 in human ECs, we treated cultured human aortic endothelial cells (HAECs) with ki8751 for 6 hours
126 and analyzed *AQP1* expression by qPCR. *AQP8* expression was not examined since it is not
127 expressed in HAECs (data not shown). Inhibition of VEGFR2 activity with 1 nM and 10 nM
128 ki8751 decreased *AQP1* mRNA expression by 31% ($p = 0.0023$, Fig. 1I) and 40% ($p = 0.1032$,
129 Fig. 1I), respectively, demonstrating cross-species conservation of VEGFR2 activity in inducing
130 *Aqp1* mRNA expression.
131 Notch signalling was inhibited using the gamma-secretase inhibitor, Dibenzazepine (DBZ),
132 which prevents proteolytic cleavage and consequently, activation of the Notch receptor (Groth et
133 al., 2010). Treatment of embryos with DBZ from 20 hpf for 6 and 24 hours significantly decreased
134 the expression of *hey1* and *hey2,* canonical targets of Notch signalling (Fig. 1J), confirming the
135 effectiveness of the drug treatment in our experiments. When compared to DMSO-treated embryos,
136 6-hour treatment with DBZ did not cause a significant change in *aqp1a.1* and *aqp8a.1* expression
137 levels (Fig. 1J). Longer treatment with DBZ for 24 hours, however, increased *aqp8a.1* expression
138 by 98% ($p < 0.0001$) while *aqp1a.1* expression was relatively unchanged (Fig. 1J). These findings
139 suggest that Notch signalling inhibits *aqp8a.1*, but not *aqp1.a*, expression.
140
141 **Aqp1a.1 and Aqp8a.1 proteins are enriched at the leading front of migrating tip cells**
142 To gain a better understanding of where within the cell Aquaporin protein functions, we generated
143 stable *Tg(fli1ep:aqp1a.1-mEmerald)*^{rk30} and *Tg(fli1ep:aqp8a.1-mEmerald)*^{rk31} zebrafish lines in
144 which ECs express Aqp1a.1 or Aqp8a.1 tagged with mEmerald, respectively. At 25 hpf, we
145 observed an accumulation of Aqp1a.1 (Fig. 2A) and Aqp8a.1 (Fig. 2B) in mCherryCAAX-positive
146 membrane clusters in the cytoplasm and filopodia of tip cells. Interestingly, many of the Aqp1a.1-
147 or Aqp8a.1-positive membrane clusters are located at the migrating front of the tip cell. Time-
148 lapse imaging capturing the process of ISV formation between 24 to 30 hpf further showed
149 sustained enrichment of Aqp1a.1 and Aqp8a.1 in clusters at the front of the tip cell as well as in
150 filopodia (Fig. 2C and D, Movie S1 and S2), suggesting that Aqp1a.1 and Aqp8a.1 may promote
151 localized water flux at the migrating edge of tip cells.
152
153 **Loss of Aqp1a.1 and Aqp8a.1 function leads to defective trunk blood vessel formation**
154 We subsequently proceeded to generate zebrafish *aqp1a.1* and *aqp8a.1* mutants to investigate the
155 function of Aquaporin-mediated water flow in blood vessel development. Using the CRISPR/Cas9

156 genome editing technique, we targeted the first exons of *aqp1a.1* and *aqp8a.1* genes. The CRISPR-
157 generating allele *aqp1a.1*^{rk28} carries a 14-bp deletion and an 8-bp insertion in the 5' end of the gene
158 leading to a premature termination codon at amino acid 76 after 1 missense amino acid (Fig. S4A-
159 B). The *aqp8a.1*^{rk29} allele carries a 4-bp deletion in the 5' end of the gene that leads to a frameshift
160 after T15 and premature termination codon at amino acid 73 after 58 missense amino acids (Fig.
161 S5A-B). Premature termination codons are often more deleterious than missense mutations
162 because they result in the loss of protein expression. Nonsense-mediated mRNA decay is a quality-
163 control mechanism that selectively degrades mRNAs harboring premature termination codons
164 (Chang et al., 2007). Using whole-mount *in situ* hybridization and qPCR analysis, we
165 demonstrated that *aqp1a.1* and *aqp8a.1* mRNA expression is significantly decreased in
166 *aqp1a.1*$^{rk28/rk28}$ (Fig. S4C-D) and *aqp8a.1*$^{rk29/rk29}$ (Fig. S5C-D) zebrafish embryos, respectively,
167 suggesting a rapid degradation of mutant mRNAs and as a result, the loss of Aquaporin protein
168 expression.

169 Although *aqp1a.1*$^{rk28/rk28}$*;aqp8a.1*$^{rk29/rk29}$ embryos look morphologically normal when
170 compared to wildtype or *aqp1a.1*$^{+/rk28}$*;aqp8a.1*$^{+/rk29}$ embryos (Fig. S8A, B, C and D), we observed
171 defects in blood vessel formation and patterning at 1 to 3 dpf. Compared to 28 hpf control embryos
172 whose ISVs have reached the dorsal roof of the neural tube and started to form the DLAV, ISVs
173 of *aqp1a.1*$^{rk28/rk28}$*;aqp8a.1*$^{rk29/rk29}$ embryos are much less developed (Fig. 3A and D) with
174 significantly reduced length (Fig. 3E and Fig. S6H and K). Single deletion of *aqp1a.1* (Fig. 3B
175 and Fig. S6F and I) or *aqp8a.1* (Fig. 3C and Fig. S6G and J) also led to defective ISV formation,
176 although the defects are less severe compared to the loss of both *aqp1a.1* and *aqp8a.1* expression.
177 Comparison of ISV length in *aqp1a.1*$^{rk28/rk28}$, *aqp8a.1*$^{rk29/rk29}$ and *aqp1a.1*$^{rk28/rk28}$*;aqp8a.1*$^{rk29/rk29}$
178 embryos shows that the loss of *aqp1a.1* leads to a greater decrease in ISV length than the loss of
179 *aqp8a.1* (Fig. 3E, Fig. S6I and J), and that the loss of both *aqp1a.1* and *aqp8a.1* resulted in the
180 greatest reduction. These observations indicate an additive effect of Aqp1a.1 and Aqp8a.1 function
181 in blood vessel development and implicate Aqp1a.1 as the more dominant Aquaporin protein in
182 EC function, in line with the higher expression of *aqp1a.1* mRNA in tip cells.

183 We next examined the embryos at 3 dpf, a stage when arterial ISVs (aISVs) and venous
184 (vISVs) are fully established and lumenized, connecting the DLAV to either the DA or PCV (Fig.
185 3F and G), respectively. Such fully established ISVs are significantly reduced in embryos when
186 *aqp1a.1*, *aqp8a.1* or both *aqp1a.1* and *aqp8a.1* are deleted. Instead, these embryos display an

187 increased number of aISVs and vISVs that fail to establish a connection to the DLAV, DA or PCV
188 (Fig. 3H – J). Quantification shows that while 19.1% of wildtype embryos display at least 1
189 incomplete ISV per embryo, this increased to 65.8% in *aqp8a.1*$^{rk29/rk29}$ embryos, 83.3% in
190 *aqp1a.1*$^{rk28/rk28}$ embryos and 92.2% in *aqp1a.1*$^{rk28/rk28}$*;aqp8a.1*$^{rk29/rk29}$ embryos (Fig. 3K). The
191 number of incomplete ISVs per embryo in *aquaporin* mutants was variable, between 1 to 6, 1 to
192 16 and 1 to 22 incomplete ISVs in *aqp8a.1*$^{rk29/rk29}$, *aqp1a.1*$^{rk28/rk28}$ and
193 *aqp1a.1*$^{rk28/rk28}$*;aqp8a.1*$^{rk29/rk29}$ embryos, respectively (Fig. S6A-D). We also found that incomplete
194 ISVs appear with higher frequency in the zebrafish trunk (ISV number 6 to 15) rather than in the
195 tail (ISV number 16 to 27, Fig. S6E). Detailed analysis revealed that most of the incomplete ISVs
196 are vISVs that are connected to the PCV but not the DLAV (Class I, 75.2%), followed by the
197 absence of aISV or vISV (Class II, 15.8%, Fig. 3L and Fig. S7A and B). A small fraction of the
198 incompletely formed vessels are aISVs that are not connected to the DA (Class IV, 2.2%, Fig.
199 S7D) or DLAV (Class V, 2.9%, Fig. S7E), or vISVs that are not connected to the DLAV (Class
200 VII, 2.68%, Fig. S7F). At some regions, there is an aISV that is not connected to the DA and a
201 vISV that is not connected to the DLAV (Class III, 1.2%, Fig. S7C).
202 As *aqp1a.1* is expressed in brain vasculature during development (Fig. S1), we examined
203 whether cerebral vasculature is also affected in *aqp1a.1*$^{rk28/rk28}$ embryos. At 4 dpf, we found that
204 the length of the dorsal longitudinal vein (DLV), a main blood vessel that supplies blood to the
205 choroid plexus (Bill and Korzh, 2014) was reduced in *aqp1a.1*$^{rk28/rk28}$ embryos (p = 0.0098, Fig.
206 S9B). Also, in 2 out of 21 *aqp1a.1*$^{rk28/rk28}$ embryos, the DLV was undeveloped (Fig. S9A and C),
207 a defect that is also observed in 50% of *vegfab*$^{-/-}$ and *vegfc*$^{-/-}$ mutant zebrafish (Parab et al., 2021).
208 In summary, our analyses suggest that in the absence of Aqp1a.1 and/or Aqp8a.1 function,
209 there is an initial delay in ISV formation during primary sprouting angiogenesis. By 3 dpf, some
210 ISVs are completely formed (Fig. S8K and M), connecting the DA or PCV to the DLAV. However,
211 the number of completely formed ISVs is significantly decreased, with the loss of Aqp1a.1 having
212 a more severe impact compared to the loss of Aqp8a.1, and the combined loss of Aqp1a.1 or
213 Aqp8a.1 having a greater deleterious effect.
214
215 **Aquaporins promote endothelial tip cell protrusion and migration**
216 To gain a better understanding of how incomplete ISV formation arise, we performed timelapse
217 imaging in zebrafish depleted of both Aqp1a.1 and Aqp8a.1 function from 21 – 22hpf, when

218 sprouting angiogenesis begins. In *aqp1a.1*$^{+/rk28}$*;aqp8a.1*$^{+/rk29}$ embryos, tip cells emerge from the
219 DA between 20 and 24 hpf (Fig. 4A) and migrate dorsally between the somite boundaries over the
220 notochord and neural tube to form primary ISVs (Fig. 4B, Movie S3). However, in
221 *aqp1a.1*$^{rk28/rk28}$*;aqp8a.1*$^{rk29/rk29}$ embryos, tip cell nuclei emerge between 22 and 28 hpf (Fig. 4A).
222 Furthermore, in some *aqp1a.1*$^{rk28/rk28}$*;aqp8a.1*$^{rk29/rk29}$ embryos, tip cells retract whereby membrane
223 protrusions do not extend dorsally in the direction of migration but withdraw into the DA so that
224 a primary ISV does not form at this location (Fig. 4C, Movie S4). These observations indicate that
225 tip cell protrusion from the DA is significantly delayed in the absence of Aqp1a.1 and Aqp8a.1
226 function.

227 We have previously demonstrated that filopodia facilitate EC migration by serving as a
228 template for lamellipodia formation (Phng et al., 2013). Lamellipodia frequently emanate laterally
229 from stable filopodia at the leading edge of tip cells, leading to rapid expansion of the filopodium,
230 increase in volume and the formation of a stable protrusion in the direction of migration (Phng et
231 al., 2013). This was similarly observed in *aqp1a.1*$^{+/rk28}$*;aqp8a.1*$^{+/rk29}$ embryos (Fig. 4D, Movie S5)
232 but not in *aqp1a.1*$^{rk28/rk28}$*;aqp8a.1*$^{rk29/rk29}$ embryos (Fig. 4E, Movie S6). Comparison of filopodia
233 dynamics in wildtype (Fig. 4F), *aqp1a.1*$^{+/rk28}$*;aqp8a.1*$^{+/rk29}$ and *aqp1a.1*$^{rk28/rk28}$*;aqp8a.1*$^{rk29/rk29}$
234 (Fig. 4G) embryos revealed a significant reduction in filopodia number (wildtype, 18.75 ±
235 5.1/100µm; *aqp1a.1*$^{+/rk28}$*;aqp8a.1*$^{+/rk29}$, 19.8 ± 6.3/100µm; *aqp1a.1*$^{rk28/rk28}$*;aqp8a.1*$^{rk29/rk29}$, 9.9 ±
236 5.2/100µm; Fig. 4H) and length (wildtype, 5.9 ± 3.2 µm; *aqp1a.1*$^{+/rk28}$*;aqp8a.1*$^{+/rk29}$, 6.2 ± 3.3 µm;
237 *aqp1a.1*$^{rk28/rk28}$*;aqp8a.1*$^{rk29/rk29}$, 4.8 ± 2.4 µm; Fig. 4I) in ECs lacking both Aqp1a.1 and Aqp8a.1.
238 function. Analysis of time-lapse images of tip cell behaviour further showed slower tip cell
239 membrane expansion at the leading edge (Fig. 4J), decreased nuclei displacement (Fig. 4K) and a
240 significant reduction in tip cell migration velocity (Fig. 4L) in *aqp1a.1*$^{rk28/rk28}$*;aqp8a.1*$^{rk29/rk29}$
241 embryos.

242 In conclusion, Aqp1a.1 and Aqp8a.1 are required for sprouting angiogenesis by promoting
243 endothelial tip cell emergence from the DA, the formation of membrane protrusions and
244 endothelial cell migration.

245

246 **Tip cell volume regulation depends on Aquaporin-mediated water influx**

247 Aquaporin channels permit bidirectional flow of water across the plasma membrane, with the
248 direction of flow determined by the osmotic gradient between the extracellular environment and

249 cell cytoplasm (Agre et al., 2002). We next sought to determine whether water flows in or out of
250 tip cells during sprouting angiogenesis. We hypothesize that water flux across the cell membrane
251 can lead to changes in tip cell volume, with water influx increasing the volume while outflow
252 decreases. To quantify tip cell volume, we injected a plasmid encoding *kdrl:mEmerald* transgene
253 into 1-cell stage wildtype or *aqp1a.1*$^{rk28/rk28}$*;aqp8a.1*$^{rk29/rk29}$ embryos to label ECs in a mosaic
254 manner. mEmerald-positive tip cells were imaged and their volume measured at 24 to 25 hpf.
255 Wildtype ECs are on average 946.6 ± 299.8 μm^3 in size (Fig. 5A and C). In the absence of both
256 Aqp1a.1 and Aqp8a.1 function (Fig. 5B), tip cell volume significantly decreased by about 24% to
257 718.4 ± 308.5 μm^3 (p = 0.0176, Fig. 5C) when compared to wildtype tip cells. This finding
258 supports water influx as the direction of water flow in tip cells during migration, and that this is
259 mediated through Aqp1a.1 and Aqp8a.1.
260 It has been proposed that water influx through Aquaporin increases the diffusion of actin
261 monomers and increases actin polymerisation (Loitto et al., 2007; Papadopoulos et al., 2008) .
262 Given that filopodia formation is dependent on actin polymerization (Mallavarapu and Mitchison,
263 1999; Ridley, 2011), we examined whether actin polymerization is perturbed in the absence of
264 Aqp1a.1 and Aqp8a.1 by quantifying the growth rate of actin bundles in tip cell filopodia by
265 tracking Lifeact-mCherry signal in the filopodia. In wildtype embryos, the average growth rate of
266 actin is 0.054 ± 0.015 µm per second whereas in *aqp1a.1*$^{rk28/rk28}$*;aqp8a.1*$^{rk29/rk29}$ embryos, the
267 growth rate is significant decreased by 47% to 0.028 ± 0.010 µm per second ($p < 0.0001$, Fig. 5D).
268 Our observations therefore support a role of zebrafish Aqp1a.1 and Aqp8a.1 in promoting actin
269 polymerisation and consequently, filopodia number and length, which are reduced in
270 *aqp1a.1*$^{rk28/rk28}$*;aqp8a.1*$^{rk29/rk29}$ embryos (Fig. 4F and G).
271 In summary, our results demonstrate a role of endothelial Aquaporins in increasing water
272 influx and as a consequence, endothelial tip cell volume and hydrostatic pressure, as well as in
273 promoting actin polymerization.
274
275 **Additive effects of actin polymerization and water influx in driving EC migration and**
276 **sprouting angiogenesis**
277 We have previously observed that ECs are still able to migrate to generate ISVs after the inhibition
278 of actin polymerization (Phng et al., 2013). In these experiments, embryos were treated with a low
279 concentration of Latrunculin B (Lat. B), an inhibitor of actin polymerization, that resulted in the

280 suppression of filopodia formation. Under such conditions, ECs can generate small membrane
281 protrusions and migrate more slowly in a directed manner to generate ISVs. How ECs are still able
282 to migrate after the inhibition of actin polymerization was unclear. As our current study
283 demonstrates a role of water inflow and hydrostatic pressure as another mechanism of cell
284 migration, we hypothesize that ECs employ water influx to migrate when actin polymerization is
285 compromised and that the depletion of both water influx and actin polymerization will result in a
286 greater inhibition of EC migration.

287 To test this hypothesis, we examined ISV development in embryos with decreased actin
288 polymerization and water inflow by treating *aqp1a.1*$^{rk28/rk28}$*;aqp8a.1*$^{rk29/rk29}$ embryos with Lat. B.
289 At 28 hpf, ISVs of wildtype embryos treated with DMSO have reached the dorsal roof of the neural
290 tube (Fig. 6A) and show an average length of 104.1 ± 13.47 µm (Fig. 6E). The treatment of
291 wildtype embryos with 0.08 µg/ml Lat. B from 20 to 28 hpf (Fig. 6B) resulted in a significant
292 decrease in ISV length (61.53 ± 23.27 µm) compared to control embryos ($p < 0.0001$, Fig. 6E). A
293 similar decrease in ISV length was also observed in *aqp1a.1*$^{rk28/rk28}$*;aqp8a.1*$^{rk29/rk29}$ embryos treated
294 with DMSO (63.75 ± 30.24 µm, Fig. 6C and E). When *aqp1a.1*$^{rk28/rk28}$*;aqp8a.1*$^{rk29/rk29}$ embryos
295 were treated with 0.08µg/ml Lat. B from 20 to 28 hpf, there was a greater decrease in the length
296 of ISV formed at 28 hpf (43.10 ± 24.42 µm, Fig. 6D and E) when compared to the inhibition of
297 actin polymerization ($p = 0.0028$) or depletion of water influx ($p < 0.0001$) alone (Movie S7).
298 These results therefore demonstrate additive functions of actin polymerization and water influx in
299 driving EC migration during sprouting angiogenesis (Fig. 6F).
300

301 **DISCUSSION**

302 In this study, we demonstrate that endothelial tip cells utilize two mechanisms of migration
303 concurrently during sprouting angiogenesis in the zebrafish - actin polymerization and hydrostatic
304 pressure. The increase in hydrostatic pressure in endothelial tip cells is generated by Aqp1a.1- and
305 Aqp8a.1-mediated water inflow. By performing detailed expression analyses, we showed that
306 *aqp1a.1* and *aqp8a.1* are differentially expressed in newly formed vascular sprouts. *Aqp1a.1* is
307 expressed earlier in the DA than *aqp8a.1* during development and in ECs destined to be tip cells.
308 In newly formed ISVs, endothelial tip cells express higher *aqp1a.1* mRNA levels while stalk cells
309 express higher *aqp8a.1* mRNA levels. In zebrafish harbouring mutations in both *aqp1a.1* and
310 *aqp8a.1*, there is delayed tip cell protrusion from the DA, decreased tip cell migration and

311 increased occurrence of truncated ISVs at 3 dpf. We further discovered that *aqp1a.1* and *aqp8a.1*
312 expression is upregulated by VEGFR2 activity, proposing that VEGFA-VEGFR2 signalling
313 employs Aquaporin function to drive sprouting angiogenesis.

314 Several lines of evidence implicate Aquaporins in facilitating water flow into endothelial
315 tip cells during sprouting angiogenesis. First, timelapse imaging showed enriched localization of
316 Aqp1a.1 and Aqp8a.1 proteins at the migrating front of tip cells, suggesting that water flow occurs
317 locally at the leading edge of the cell. Secondly, single cell analyses revealed Aqp1a.1- and
318 Aqp8a.1-deficient tip cells have decreased cell volume, impaired expansion of cell membranes at
319 the leading edge and decreased generation of stable cell protrusions. These observations implicate
320 water flow into tip cells, leading to increased cell volume. Due to the incompressible property of
321 water within an enclosed compartment such as the cell, water influx will lead to a rise in hydrostatic
322 pressure. At the leading edge of tip cells, increased hydrostatic pressure would expand and deform
323 membranes to generate protrusions. Additionally, water influx can reduce cytoplasmic viscosity
324 and increase spacing between the plasma membrane and the underlying actin cytoskeleton,
325 promoting actin monomer diffusion, actin polymerization and the generation of membrane
326 protrusions to facilitate cell migration (Boer et al., 2023; Loitto et al., 2009).

327 A key finding in this study is the demonstration that endothelial tip cells employ hydrostatic
328 pressure as a second mechanism of cell migration *in vivo*. In a previous study, we discovered that
329 ECs continue to migrate when actin polymerization is inhibited and in the absence of filopodia
330 (Phng et al., 2013). Here, we show that hydrostatic pressure is the driving force for EC migration
331 in the absence of actin-based force generation. When both mechanisms are perturbed, there is a
332 greater impairment in EC migration (Fig. 6D and E). This finding highlights the importance of
333 hydrostatic pressure as an additional mechanism that reinforces actin-based cell shape changes and
334 motility to ensure robust migration and formation of new blood vessels in complex three-
335 dimensional environments. Such dual mode migration is advantageous when blood vessels
336 develop in physically confined spaces such as in the zebrafish trunk, where ECs must emerge from
337 the DA and migrate within somite boundaries and over tissues such as the notochord and neural
338 tube to form ISVs. Such dependence on water flow in cell migration under confined
339 microenvironment has been reported in human MDA-MB-231 breast cancer cells and mouse S180
340 sarcoma cells, which show cell migration persistence in narrow channels after inhibition of actin
341 polymerization or myosin II-mediated contractility (Stroka et al., 2014). In this context, AQP5

342 mediates water flow and the decrease or increase in AQP5 expression suppresses or enhances,
343 respectively, cancer cell migration (Chae et al., 2008; Jung et al., 2011; Stroka et al., 2014).
344 Our findings on the endothelial function of zebrafish Aqp1a.1, which is homologous to
345 mammalian AQP1, corroborate previous studies demonstrating a function of AQP1 in promoting
346 cell migration. In tumour bearing AQP1-null mice, there is reduced tumour angiogenesis and
347 AQP1-deficient ECs display reduced migration in an *in vitro* wound healing assay (Maltaneri et
348 al., 2020; Saadoun et al., 2005). In chick, AQP1 expression levels affect neural crest cell migration
349 speed and direction by regulating filopodia length and stability (McLennan et al., 2019). The
350 regulation of membrane protrusions has also been demonstrated for other Aquaporin proteins. For
351 example, AQP9 weakens membrane-cytoskeleton anchorage and promote formation of membrane
352 protrusions such as filopodia and blebs (Karlsson et al., 2013; Loitto et al., 2007). We also
353 demonstrate for the first time a role of Aqp8a.1 in promoting EC migration and sprouting
354 angiogenesis in the zebrafish. However, its mammalian ortholog, AQP8, was shown to inhibit
355 migration of colorectal cancer cell lines *in vitro* (Wu et al., 2017), suggesting cell- and context-
356 dependent function of AQP8 in the regulation of cell migration.
357 A central determinant of water movement is the osmotic gradient across the membrane,
358 with water flowing in the direction of higher solute concentration. Given a crucial role of water
359 flow in regulating cell volume, shape and migration, it is also important to understand the function
360 and distribution of ion channels, exchangers and transporters and water channels that generate an
361 osmotic gradient across the cell. This is reflected in a growing number of studies demonstrating a
362 role of ion transporters in cell migration. In neutrophils, the increase in cell volume and
363 potentiation of cell migration depend on the sodium-proton exchanger 1 (NHE1) and the chloride-
364 bicarbonate exchanger 2 (AE2) (Nagy et al., 2023) . In T cells, chemokine-induced migration
365 depends on ion influx via SLC12A1, and water influx via AQP3 (Boer et al., 2023). In tumour
366 cells migrating in narrow channels, the establishment of a polarized distribution of Na^+/H^+ pumps
367 and Aquaporin proteins in cell membranes is required for net inflow of ions and water at the
368 leading edge and net outflow at the trailing edge (Stroka et al., 2014). We have also observed
369 enrichment of Aqp1a.1 and Aqp8a.1 proteins in ECs, at the leading edge of migrating endothelial
370 tip cells as well as apical membranes during lumen formation (not shown). This leads to the
371 question of how Aquaporin localisation is regulated as this will determine the site of increased
372 water flow and hydrostatic pressure. The rapid changes in subcellular localization of mammalian

373 Aquaporins upon stimulation occurs mainly via trafficking to and from the plasma membrane
374 (Markou et al., 2022), and can lead to changes in the amount of Aquaporin protein in the plasma
375 membrane. The regulation of AQP subcellular relocalization via calmodulin- and/or
376 phosphorylation-dependent mechanisms has been implicated for AQP0-5 and AQP7-9 (Markou et
377 al., 2022). For example, rapid translocation of AQP1 to plasma membrane upon a hypotonic
378 stimulus is dependent on calmodulin activation and phosphorylation by protein kinases C (PKC)
379 (Conner et al., 2012). Phosphorylation of AQP2 by protein kinase A (PKA) is required for
380 vasopressin-stimulated relocalization of AQP2 from storage vesicles to the plasma membrane
381 (Noda and Sasaki, 2005). Subcellular localization of AQP8 in hepatocytes is also regulated by
382 PKA and PI3K signalling (Gradilone et al., 2005, 2003). In mouse neutrophils, exposure to a
383 chemotactic gradient caused translocation of AQP9 to the leading edge of the cell that is mediated
384 by PKC-dependent phosphorylation (Karlsson et al., 2011). Further work is needed to elucidate
385 the mechanism of Aqp1a.1 and Aqp8a.1 protein distribution in ECs and which ion transporters are
386 expressed in ECs to regulate the ion movement and cell migration.

387 In this study, we have assumed that the function of Aqp1a.1 and Aqp8a.1 is a result of
388 water permeation based on previous studies demonstrating water molecules flowing through
389 mammalian AQP1 (Preston et al., 1992; Zeidel et al., 1992) and AQP8 (Liu et al., 2006; Ma et al.,
390 1997) as well as through their zebrafish orthologs Aqp1a.1 and Aqp8a.1 (Tingaud-Sequeira et al.,
391 2010). However, AQP1 and AQP8 are not water-specific channels. AQP1 can conduct unpolar
392 gases carbon dioxide (Nakhoul et al., 1998; Prasad et al., 1998; Wang et al., 2007) and nitric oxide
393 (Herrera et al., 2006; Herrera and Garvin, 2007), and in zebrafish, Aqp1a.1 also mediates the
394 transfer for small gaseous molecules such as carbon dioxide and ammonia (Talbot et al., 2015).
395 AQP8 is permeable to ammonia (Jahn et al., 2004; Liu et al., 2006) and is present in the inner
396 mitochondrial membrane of different cells (Calamita et al., 2005), where it is suggested to mediate
397 ammonia transport rather than water fluxes (Soria et al., 2010). Among the three Aqp8 paralogs in
398 teleost, Aqp8a.1 and Aqp8a.2 are also permeable to urea (Tingaud-Sequeira et al., 2010) and
399 Aqp8b was shown to act mainly as a mitochondrial H_2O_2 channel (peroxiporin) in activated marine
400 and freshwater teleost spermatozoa (Chauvigné et al., 2021, 2015). Nevertheless, because water
401 movement flows up an osmotic gradient, increased entry of ions into the cell through Aquaporins
402 will also trigger water inflow.

403 In summary, our study highlights the role of water influx and hydrostatic pressure as
404 another force-generating mechanism utilized by cells to build tissues during animal development.
405 We demonstrate that endothelial tip cells employ both actin polymerization and hydrostatic
406 pressure for robust sprouting angiogenesis. As morphogenetic events are governed by a
407 coordination of cell shape changes, cell migration and rearrangements, we envision that the
408 shaping and formation of other tissues will also depend on Aquaporin function and changes in
409 hydrostatic pressure.
410
411 **METHODS**
412 **Zebrafish maintenance and stocks.**
413 Zebrafish (*Danio rerio*) were raised and staged according to established protocols (Kimmel et al.,
414 1995). Transgenic lines used in this work are *Tg(kdrl:EGFP)*^{s843} (Jin et al., 2005) ,*Tg(fli1a:H2B-*
415 *EGFP)*^{ncv69} [re-named in ZFIN as *Tg(fli1:zgc:114046-EGFP)*] (Ando et al., 2019), *Tg(fli1:Lifeact-*
416 *mCherry)*^{ncv7} (Wakayama et al., 2015), *Tg(fli1:myr-mCherry)*^{ncv1} (Fukuhara et al., 2014),
417 *Tg(fli1ep:EGFP-PLC1δPH)*^{rk26} (Kondrychyn et al., 2020), *Tg(fli1:h2bc1-mCherry)*^{ncv31} (Nakajima
418 et al., 2017), *Tg(kdrl:ras-mCherry)*^{s916} (Hogan et al., 2009). Zebrafish were maintained on a 12-
419 hour light/12-hour dark cycle, and fertilized eggs were collected and raised in E3 medium at 28^0C.
420 To inhibit pigmentation in embryos older than 24 hpf, 0.003% *N*-Phenylthiourea (Sigma-Aldrich)
421 in E3 medium was used. All animal experiments were approved by the Institutional Animal Care
422 and Use Committee at RIKEN Kobe Branch (IACUC).
423
424 **Plasmids and oligonucleotides.**
425 All DNA constructs used in this study were generated by using In-Fusion HD Cloning kit (Takara
426 Bio Inc.). Plasmid *mEmerald-N1* was a gift from Michael Davidson (Addgene plasmid #53976).
427 Plasmids *pDsChLexOG* (Emelyanov and Parinov, 2008) containing terminal *cis*-required
428 sequences of the *Ds* transposon from maize was a generous gift from Sergei Parinov. A detailed
429 information regarding plasmids and primers used in this study can be found in Supplementary
430 Tables 1 and 2, respectively.
431
432 **Cloning of *aqp1a.1* and *aqp8a.1* genes.** Total RNA was isolated from 1-day old zebrafish
433 embryos with TRI Reagent using Direct-zol™ RNA MicroPrep kit (Zymo Research) according to

434 the manufacturer's protocol. The first-strand cDNA was synthesized from 1 µg of a total RNA by
435 oligo(dT) priming using the SuperScript III First-Strand synthesis system (Invitrogen) according
436 to the manufacturer's protocol. Amplification of cDNAs was performed using a high-fidelity
437 KOD-Plus-Neo DNA polymerase (Toyobo, Japan) and resulting PCR products were cloned using
438 NEB® PCR Cloning kit (New England BioLabs). Positive clones and plasmids were verified by
439 DNA sequencing.
440
441 **Mosaic expression of DNA constructs and transgenic lines generation.**
442 To establish *Tg(fli1ep:aqp1a.1-mEmerald)*^{rk30} and *Tg(fli1ep:aqp8a.1-mEmerald)*^{rk31} transgenic
443 lines, *Tol2*-based plasmids (10 ng/µl) were co-injected into one-cell stage zebrafish embryos with
444 *Tol2* transposase mRNA (100 ng/µl) transcribed from Not*I*-linearized *pCS-TP* plasmid (a gift from
445 Koichi Kawakami, National Institute of Genetics, Japan) using the mMESSAGE mMACHINE
446 SP6 kit (Invitrogen). Injected embryos were raised to adults and screened for germline
447 transmission to establish a stable transgenic line. For mosaic expression of DNA construct, *Ds*-
448 based *kdrl:mEmerald* plasmid (10 ng/µl) was co-injected into one-cell stage zebrafish embryos
449 with *Ac* transposase mRNA (100 ng/µl) transcribed from Bam*HI*-linearized *pAc-SP6* plasmid
450 (Emelyanov et al., 2006) using the mMESSAGE mMACHINE SP6 kit (Invitrogen). Embryos
451 were analyzed at 25-26 hpf after injections.
452
453 ***In vivo* cell volume analysis.**
454 Single-cell labelling of ECs in ISVs was achieved by mosaic expression of *pDs-kdrl:mEmerald*
455 plasmid in wild type or *aqp1a.1*$^{rk28/rk28}$*;aqp8a.1*$^{rk29/rk29}$ mutant *Tg(fli1:Lifeact-mCherry)*^{ncv7}
456 transgenic embryos. Embryos were imaged at 25-26 hpf with an Olympus UPLSAPO 60x/NA 1.2
457 water immersion objective with optical Z planes interval of 0.26 µm. Cell volume was measured
458 with Huygens Essential 22.10 software (Scientific Volume Imaging B.V.) using object analyzer
459 tool with manual adjustment of threshold.
460
461 **Generation of zebrafish *aqp1a.1* and *aqp8a.1* mutants.**
462 Aquaporins mutants were generated by CRISPR/Cas9-mediated mutagenesis. A guide RNAs
463 (gRNAs) targeting the first exons of *aqp1a.1* and *aqp8a.1* (Fig. S4 and S5) were generated by
464 using cloning-independent protocol (Gagnon et al., 2014). Briefly, to generate templates for gRNA

465 transcription, a 60-base oligodeoxynucleotides containing the SP6 promoter sequence, the gene-
466 specific sequence (*aqp1a.1*: 5'-GACAGCTGGCCAGCAGACCC-3'; *aqp8a.1*: 5'-
467 GATGTCTCCCCCATCGCCCG-3') and 23-base overlap region was annealed to an 80-base
468 constant oligodeoxynucleotide encoding the reverse-complement of the tracrRNA tail. The ssDNA
469 overhangs were filled-in with T4 DNA polymerase (New England BioLabs) to generate dsDNA.
470 The gRNAs were *in vitro* transcribed using MEGAScript SP6 kit (Invitrogen), DNase treated and
471 purified with RNA Clean and Concentrator kit (Zymo Research). The gRNAs were quality-
472 checked by running 1 µg of the product on a 2% TBE-agarose gel. Cas9/gRNA RNP complex was
473 assembled just prior to injection and after 5 min incubation at room temperature 200 pg of Cas9
474 protein (Invitrogen) and 200 pg of gRNAs (100 pg of each, *aqp1a.1* gRNA and *aqp8a.1* gRNA)
475 were co-injected into one-cell stage *Tg(fli1:myr-mCherry)*^{ncv1} embryos. Such dose produced over
476 70% embryos survival post-injection showed CRISPR/Cas9-induced somatic *aqp1a.1* and
477 *aqp8a.1* gene mutations. F_0 founders were identified by outcrossing CRISPR/Cas9-injected fish
478 with wild type fish and screening the offspring for mutations at 2 dpf using Sanger sequencing.
479 We found one F_0 fish with germline transmitted mutations in both *aqp1a.1* and *aqp8a.1* genes and
480 outcrossed it with *Tg(fli1:myr-mCherry)*^{ncv1} and *Tg(fli1a:H2B-EGFP)*^{ncv69} transgenic fish to
481 establish F_1 generation of heterozygotes. A 55 F_1 fish were genotyped to identify 4 *aqp1a.1*$^{+/rk28}$,
482 *11 aqp8a.1*$^{+/rk29}$ and 12 *aqp1a.1*$^{+/rk28}$*;aqp8a.1*$^{+/rk29}$ heterozygote fish. Subsequently, F_1
483 heterozygote fish were in-crossed to establish a single and double homozygote fish.
484
485 **DNA isolation and genotyping.** Genomic DNA was isolated from either embryos or fin clips
486 using HotSHOT method (Meeker et al., 2007). To identify genomic lesions, the following primers
487 were used: aqp1a1-fwd (5'-CGCCTCCAGATTCATTAGCAGGA-3') and aqp1a1-rev (5'-
488 GTAAGTGAACTGCTGCCAGTGA-3') to amplify a 550 bp fragment, and aqp8a1-fwd (5-
489 GGATCAATTGAGTTGCATAACAGAC-3') and aqp8a1-rev (5'-
490 CTGTAATGTAGACTTGTAAAGTGGA-3') to amplify a 638 bp fragment. Mutations were
491 assessed by direct sequencing of purified PCR products.
492
493 **Quantitative real-time PCR.**
494 Total RNA from whole embryos was isolated with TRI reagent using Direct-zol RNA MicroPrep
495 kit (Zymo Research) according to the manufacturer's protocol, including on-column DNA

496 digestion. RNA was quantified using a NanoDrop 1000 spectrophotometer (ThermoFisher
497 Scientific, USA). cDNA was synthesized from 300 ng of purified RNA using LunaScript RT
498 SuperMix kit (New England BioLabs) according to the manufacturer's protocol. Amplification of
499 target cDNA was performed in technical triplicate of three biological replicates using the SYBR
500 green methods. Each qPCR reaction mixture contained 5 µL 2x Luna Universal qPCR master mix
501 (New England BioLabs), 1 µL cDNA (2-fold dilution), 0.2 µL antarctic thermolabile UDG (New
502 England BioLabs) and 250 nM each primer to a final volume of 10 µL. Reactions were run in 384-
503 well plates (Applied Biosystems) using the QuantStudio 5 Real-Time PCR system (Applied
504 Biosystems) with the following thermal cycling conditions: initial UDG treatment at 25^0C for 2
505 minutes, UDG inactivation at 50^0C for 5 min and denaturation at 95^0C for 1 minutes, followed by
506 45 cycles of 15 sec at 95^0C, 30 sec at 60^0C with a plate read at the end of the extension step.
507 Control reactions included a no-template control (NTC) and a no-reverse transcriptase control
508 (NRT). Dissociation analysis of the PCR products was performed by running a gradient from 60
509 to 95^0C to confirm the presence of a single PCR product. Amplification data was analyzed using
510 QuantStudio Design and Analysis software v1.5.3 (Applied Biosystems) and relative fold change
511 was calculated using Pfaffl method (Pfaffl, 2001) and normalized to *gapdh* expression (as an
512 internal control). Primers are listed in Supplementary Table 2. Two embryos were used in each
513 biological replicate to generate an average value that was used to calculate the final mean ± SD
514 from two or three independent experiments.
515
516 **RNA *in situ* hybridization.**
517 **RNAscope *in situ* hybridization.** RNAscope® *in situ* hybridization was conducted by using
518 RNAscope Multiplex Fluorescent Reagent kit v2 (Advanced Cell Diagnostics). We adapted
519 manufacture's protocol designed for samples mounted on slides and protocol developed for whole-
520 mount embryo samples (Gross-Thebing et al., 2014). For each experimental point, 5 embryos were
521 processed in one 1.5 ml Eppendorf tube. Briefly, 20 and 22 hpf old embryos were manually
522 dechorionated and fixed in freshly prepared 4% methanol-free PFA in PBS for 1 hour at room
523 temperature. After fixation embryos were washed three times in PBS containing 0.01% Tween-20
524 (PBST), dehydrated stepwise in 5-min washes in a series of increasing methanol concentrations
525 (25%, 50%, 75%, 100%) in PBS and then stored in 100% methanol at -20^0C before use them for
526 hybridization. The methanol-stored embryos were incubated with 5% H_2O_2 in methanol for 20 min

527 at room temperature and then rehydrated stepwise in 5-min washes in series of decreasing
528 methanol concentrations (75%, 50%, 25%) in PBS, followed by three times 5-min washes in PBST.
529 Embryos were permeabilized in 2 drops of RNAscope® Protease III for 15 min, rinsed three times
530 with PBST and hybridized with RNAscope target probes overnight at 40^0C in water bath. After
531 hybridization probes were recovered and embryos were washed three times with 0.2x SSCT
532 [0.01% Tween-20 in SSC] at room temperature, re-fixed with 4% PFA for 10 min, and washed
533 three times with 0.2x SSCT. For RNA detection, the embryos were first hybridized with three
534 different amplifier solution for 30 min (Amp1, and Amp2) and 15 min (Amp3) in a water bath at
535 40^0C. After each hybridization step, the embryos were washed three times with 0.2x SSCT for 15
536 min at room temperature. To develop signal of each probe, the embryos were sequentially
537 incubated in a water bath at 40^0C with: (i) the horseradish peroxidase (HRP) for 15 min, (ii) TSA
538 fluorophore for 30 min and (iii) the HRP blocker for 15 min. After each incubation step, the
539 embryos were washed three times with 0.2x SSCT for 15 min at room temperature. HRP step is
540 linked to a probe channel, we first developed C1 probe, *Dr-aqp1a.1* (Advanced Cell Diagnostics)
541 using HRP-C1 and TSA Vivid Fluorophore 520 (Tocris, dilution 1:1500), and then C3 probe, *Dr-*
542 *aqp8a.1* (Advanced Cell Diagnostics) using HRP-C3 and TSA Vivid Fluorophore 650 (Tocris,
543 dilution 1:1500). Nuclei were counterstained with DAPI ready-to-use solution overnight at 4^0C.
544 Prior to imaging embryos were rinsed in PBST and kept in 70% glycerol in PBS. Images were
545 acquired using Olympus FV3000 confocal microscope and an Olympus UPlanXApo 60x/NA 1.42
546 oil immersion objective.
547 **Chromogenic *in situ* hybridization.** Chromogenic *in situ* hybridization was conducted according
548 to standard protocol (Thisse and Thisse, 2007) with minor modifications. For each experimental
549 point, 10 embryos were processed in one 1.5 ml Eppendorf tube. Briefly, 30, 48, 72 and 96 hpf old
550 embryos were manually dechorionated and fixed in freshly prepared 4% methanol-free PFA in
551 PBS (pH 7.4) at 4^0C overnight. After fixation embryos were washed three times in PBS containing
552 0.1% Tween-20 (PBST), dehydrated stepwise in 5-min washes in a series of increasing methanol
553 concentrations (25%, 50%, 75%, 100%) in PBS and then stored in 100% methanol at -20^0C before
554 use them for hybridization. The methanol-stored embryos were rehydrated stepwise in 5-min
555 washes in series of decreasing methanol concentrations (75%, 50%, 25%) in PBS followed by
556 three times 5-min washes in PBST, and permeabilized 20 min with 10 µg/mL proteinase K
557 (ThermoFisher Scientific). Hybridization was carried out in buffer [50% formamide, 5x SSC, 50

558 g/mL heparin, 500 g/mL tRNA (Roche) and 0.1% Tween-20] containing 5% dextran sulfate
559 (MW=500 kDa) at 69^0C overnight. After stringency wash, the specimens were blocked with 2%
560 blocking reagent (Roche) in maleic acid buffer [100 mM maleic acid, 150 mM NaCl, 50 mM
561 $MgCl_2$ and 0.1% Tween-20, pH 7.5] and incubated overnight with anti-digoxigenin antibody,
562 conjugated with alkaline phosphatase (dilution 1:5000, Roche) at 4^0C. For detection of alkaline
563 phosphatase, specimens were incubated in staining buffer [50 mM Tris-HCl, 50 mM NaCl, 25 mM
564 $MgCl_2$, 2% Polyvinyl alcohol and 0.1% Tween-20, pH 9.5] containing 375 µg/mL nitro-blue
565 tetrazolium chloride (Roche) and 175 µg/mL 5-bromo-4-chloro-3'-indolyl-phosphate (Roche).
566 Embryos were cleared in 70% glycerol overnight and imaged using Leica M205FA microscope.
567 **RNA probe synthesis.** The cDNA-containing vectors were linearized with appropriate restriction
568 enzymes (detailed maps of vectors will be provided upon request) and used as a template for RNA
569 probe synthesis. Sense and antisense RNA probes were synthesized using MEGAscript SP6 or T7
570 kits (Invitrogen) and digoxigenin (DIG)-labeled rNTPs (Roche) according to the manufacturer's
571 protocol and purified using RNA Clean and Concentrator kit (Zymo Research). The following
572 sense and antisense DIG-labeled riboprobes were generated: (i) *aqp1a.1*, 1.1 kb long probe
573 comprised 121 nt of 5'UTR, 783 nt of the open reading frame (ORF) and 207 nt of 3'UTR; (ii)
574 *aqp8a.1*, 0.8 kb long probe comprised 17 nt of 5'UTR, 783 nt of ORF and 30 nt of 3'UTR. Sense
575 probes showed no specific or unspecific staining (data not shown).
576 **Image processing.**
577 Chromogenic and RNAscope *in situ* hybridization images were processed using ImageJ software
578 (NIH, version 2.9.0/1.53t) with brightness and contrast adjustments. Z-stacks of fluorescent
579 images are presented as maximum intensity projections.
580 **Analysis of mRNA expression in tip and stalk cells.**
581 Embryos were mounted on slide and imaged using Olympus FV3000 confocal microscope and
582 Olympus UPlanXApo 60x/NA 1.42 oil immersion objective. Maximum intensity projection of z-
583 stacks was used to determine the level of cellular fluorescence in ImageJ. The tip and stalk cells
584 were selected using freehand selection tool, "mean grey value", "area" and "integrated density" in
585 each ROI were measured first for channel 1 (aqp1a.1). A region next to cell that has no
586 fluorescence was selected as background and measured. The step was repeated for channel 2
587 (aqp8a.1) on the same ROIs. Two parameters were calculated for each channel, (i) the corrected
588 total cell fluorescence, CTCF=Integrated Density – (Area of selected cell x Mean fluorescence of

589 background) and (ii) ratio, R=CTCF of tip cell/CTCF of stalk cell. We consider that if R <0.9,
590 expression is lower in tip cell, if R=0.9-1.1, expression is equal in tip and stalk cells, if R>1.1,
591 expression is higher in tip cell.
592
593 **Imaging.**
594 For live confocal imaging, embryos were mounted in 0.8% low-melt agarose (Bio-Rad) in E3
595 medium containing 0.16 mg/mL Tricaine (Sigma-Aldrich) and 0.003% phenylthiourea (Sigma-
596 Aldrich) in glass bottom 35-mm dishes (MatTek). Confocal Z-stacks were acquired using an
597 inverted Olympus IX83/Yokogawa CSU-W1 spinning disc confocal microscope equipped with a
598 Zyla 4.2 CMOS camera (Andor) and Olympus UPLSAPO 40x/NA 1.25 or 30x/NA 1.05 silicone
599 oil immersion objectives. Bright-field images were acquired on Leica M205FA microscope.
600 Images were processed using ImageJ software (NIH, version 2.9.0/1.53t).
601
602 **Analysis of cell and nuclei migration.**
603 *aqp1a.1*$^{+/rk28}$*;aqp8a.1*$^{+/rk29}$ and *aqp1a.1*$^{rk28/rk28}$*;aqp8a.1*$^{rk29/rk29}$ embryos on *Tg(fli1a:H2B-*
604 *EGFP)*^{ncv69}*;(fli1:Lifeact-mCherry)*^{ncv7} double transgenic background were imaged from 21 to 30
605 hpf with time interval 6 min using Olympus UPLSAPO 30x/NA 1.05 silicon oil immersion
606 objective. We tried to mount both heterozygote and mutant embryos on the same dish (1 het plus
607 2 mut, or 2 het plus 2 mut) to image embryos on the same experimental conditions. Acquired time-
608 lapse images were registered using HyperStackReg plugin in ImageJ, tip cell and nuclei were
609 tracked using Manual Tracking plugin and velocity was calculated.
610
611 **Analysis of grow rate of actin bundles in filopodia.**
612 Wild type and *aqp1a.1*$^{rk28/rk28}$*;aqp8a.1*$^{rk29/rk29}$ embryos on *Tg(fli1ep:EGFP-*
613 *PLC1δPH)*^{rk26}*;(fli1:Lifeact-mCherry)*^{ncv7} double transgenic background were imaged starting from
614 25 hpf for 10 min with time interval 30 sec using Olympus UPLSAPO 60x/NA 1.2 water
615 immersion objective. Actin bundles growth was tracked using Manual Tracking plugin and
616 velocity was calculated.
617
618 **Analysis of filopodia number and length.**

619 Wild type, *aqp1a.1*$^{+/rk28}$*;aqp8a.1*$^{+/rk29}$ and *aqp1a.1*$^{rk28/rk28}$*;aqp8a.1*$^{rk29/rk29}$ embryos on
620 *Tg(fli1ep:EGFP-PLC1δPH)*^{rk26}*;(fli1:Lifeact-mCherry)*^{ncv7} double transgenic background were
621 imaged starting from 24 hpf for 30 min with time interval of 50 sec using Olympus UPLSAPO
622 60x/NA 1.2 water immersion objective. In a single image we counted filopodia number per vessel,
623 measured membrane length and calculated filopodia number.
624
625 **Chemical treatment.**
626 Latrunculin B (Merck Millipore) was dissolved in DMSO to 1 mg/ml and stored at -20^{0}C.
627 Dibenzazepine (YO-01027) (Selleck Chemicals) was prepared as 10 mM solution in DMSO and
628 stored at -80^{0}C. Ki8751 (Selleck Chemicals) was prepared as 5 mM solution in DMSO and stored
629 at -80^{0}C. All compounds were diluted to the desired concentration in E3 medium.
630
631 **Statistical analysis.**
632 Statistical analysis was performed using Prism software version 10.2.0 (GraphPad). The variance
633 between the mean values of two groups was evaluated using the unpaired Student's *t*-test. For
634 assessment of more than three groups, we used one-way analysis of variance (ANOVA) test. A *P*
635 value of <0.05 was considered statistically significant. Statistic details can be found in each figure
636 legend.
637
638 **Cell culture.**
639 Adult human aortic endothelial cells (HAEC) (Lonza, lot-20TL231227) were cultured in EGM
640 medium (Lonza) and used at passage 3. Cells were seeded in EBM medium (Lonzo) supplemented
641 with 2% FBS (Gibco) at 4 x 10^5 cells/well on 24-well plate (Trueline) coated with 5 μg/ml
642 fibronectin (Sigma-Aldrich). Cells were treated with either 0.01% DMSO or different
643 concentrations of Ki8751 inhibitor for 6 hours. Cells were lysed with TRI reagent and RNA was
644 isolated using Direct-zol RNA MicroPrep kit (Zymo Research).
645
646 **Single-cell RNA sequencing.**
647 ECs were isolated from *Tg(kdrl:EGFP)*^{s843} transgenic embryos. Cell sorting was carried out with
648 FACSAriaII Cell Sorter (BD Bioscience). Single-cell suspension was loaded into the 10X
649 Chromium system and cDNA libraries were constructed using Chromium Next GEM Single Cell

650 3′ GEM, Library and Gel Bead Kit v2 (10X Genomics) according to manufacturer's protocol.
651 Library was sequenced on the Illumina HiSeq 1500 Sequencer (Illumina, USA). Cell Ranger v2.1
652 was used to de-multiplex raw base call (BCL) files generated by Illumina sequencers into FASTQ
653 files, perform the alignment, barcode counting, and UMI counting. Sequencing reads were mapped
654 to the zebrafish genome assembly (GRCz11, Ensembl release 92). Further analyses were
655 performed using Seurat package49 (version 4.3.0) in R software (https://www.r-project.org). The
656 expression matrices were first filtered by keeping genes that are expressed in a minimum of 3 cells
657 and cells that expressed a minimum of 200 genes for downstream analysis. The data were then
658 normalized using NormalizeData function which normalizes the gene expression for each cell by
659 the total expression counts. To correct for batch effect between the data from the two-time points,
660 the rpca method in the Seurat package was applied to integrate the data. The top 2000 variable
661 genes identified using the vst method in FindVariableFeatures function were used for principal
662 component analysis in RunPCA function, and the first 30 principal components were used for
663 visualization analysis with Uniform Manifold Approximation and Projection (UMAP) method,
664 and in FindNeighbors function analysis. The cell clustering resolution was set at 0.5 in
665 FindClusters function.
666
667 **Acknowledgements**
668 We thank members of the Phng Lab, Y-C. Wang and S. Thukral for discussions and suggestions;
669 G. Chen, E. Taniguchi, RIKEN BDR Research Aquarium and RIKEN Kobe BioImaging Facilities
670 & Factory for technical assistance; J. Vermot, M. Francois and A. Yap for comments on the
671 manuscript. This work was supported by core funding from RIKEN BDR (to L.K.P.), RIKEN
672 BDR-Otsuka Pharmaceutical Collaboration Center (I.K.), the Naito Foundation (L.K.P.), the JSPS
673 Grants-in-Aid for Scientific Research (KAKENHI) grants (22H02624, 22H05168 to L.K.P;
674 22K06244 to I.K.), Swedish Research Council (2015-00550 to C.B.); Swedish Cancer Society
675 (2018/449, 2018/1154 to C.B.); Knut and Alice Wallenberg Foundation (2020.0057, 2018.0218 to
676 C.B.); Swedish Brain Foundation (ALZ2019-0130, ALZ2022-0005 to C.B.); the Leducq
677 Foundation (22CVD01, 23CVD02 to C.B.) and the Innovative Medicines Initiative (IM2PACT-
678 807015 to C.B.)
679
680 **Authorship contributions**

681 Conceptualization: L.K.P.; Methodology: I.K., H.W. and L.K.P.; Formal analysis: I.K. and L.H.;
682 Resources: C.B. and L.K.P.; Writing: I.K. and L.K.P; Supervision: L.K.P.
683
684 **Declaration of interests**
685 The authors declare no competing interests.
686
687 **Figure legends**
688
689 **Figure 1. Differential expression of *aqp1a.1* and *aqp8a.1* mRNAs in tip and stalk cells.**
690 (A-F) Detection of *aqp1a.1* and *aqp8a.1* mRNA by RNAscope *in situ* hybridization in 20 (A - D)
691 and 22 (E and F) hpf zebrafish embryos. Representative maximum intensity projection of confocal
692 z-stacks of tip and stalk cells sprouting from DA are shown (n = 9 embryos, 2 independent
693 experiments). B and F show magnified region of a tip cell from a 20 and 22 hpf zebrafish,
694 respectively (tip cell and EC nuclei in the DA are outlined). Scale bar, 10 µm (B and F) and 40 µm
695 (A, C - E).
696 (G) Percentage of vascular sprouts with differential expression of *aqp1a.1* and *aqp8a.1* mRNAs
697 in tip and stalk cells in 22 hpf zebrafish (n=23 sprouts from 8 embryos, 2 independent experiments).
698 (H) qPCR analysis of *aqp1a.1* and *aqp8a.1* expression in zebrafish embryos treated with 0.01%
699 DMSO or 1 µM ki8751 at 20 hpf for 6 or 24 hours (n = 3 independent experiments).
700 (I) qPCR analysis of *AQP1* gene expression in HAECs treated with 0.01% DMSO or 1 nM and 10
701 nM ki8751 for 6 hr (n = 2 independent experiments).
702 (J) qPCR analysis of *aqp1a.1* and *aqp8a.1* gene expression in the zebrafish embryos treated with
703 0.1% DMSO or 10 µM DBZ at 20 hpf for 6 or 24 hr (n = 2 independent experiments). In panels
704 H-J, gene expressions are shown relative to *gapdh* expression and data are presented as mean ±
705 SD; statistical significance was determined by Brown-Forsythe and Welch ANOVA tests with
706 Dunnett's multiple comparisons test; ns $p>0.05$, $^{**}p<0.01$, $^{***}p<0.001$, and $^{****}p<0.0001$. DA,
707 dorsal aorta; PCV, posterior cardinal vein.
708 See also Fig. S3.
709
710 **Figure 2. Aquaporin proteins are enriched at the leading front of migrating cells.**

711 (A and B) Representative maximum intensity projection confocal z-stacks of endothelial tip cells
712 of 25 hpf *Tg(fli1ep:aqp1a.1-mEmerald)*^{rk30}*;(kdrl:ras-mCherry)*^{s916} (A) and *Tg(fli1ep:aqp8a.1-*
713 *mEmerald)*^{rk31}*;(kdrl:ras-mCherry)*^{s916} (B) embryos. Scale bar, 20 µm.
714 (C and D) Still images from time-lapse movies of migrating tip cells from *Tg(fli1ep:aqp1a.1-*
715 *mEmerald)*^{rk30} (C) and *Tg(fli1ep:aqp8a.1-mEmerald)*^{rk31} (D) embryos. Movies were taken from 24
716 to 30 hpf. Black arrowheads, Aquaporin protein localization at the leading edge of migrating tip
717 cells. Arrows, Aquaporin localization in filopodia. Time, h:min. Scale bar, 5 µm.
718 See also Movie S1 and S2.
719
720 **Figure 3. Loss of Aquaporin function leads to defective trunk vessel formation.**
721 (A-D) Representative maximum intensity projection confocal z-stacks of 28 hpf
722 *aqp1a.1*$^{+/rk28}$*;aqp8a.1*$^{+/rk29}$ (A), *aqp1a.1*$^{rk28/rk28}$ (B), *aqp8a.1*$^{rk29/rk29}$ (C) and
723 *aqp1a.1*$^{rk28/rk28}$*;aqp8a.1*$^{rk29/rk29}$ (D) embryos.
724 (E) Quantification of ISV length in 28 hpf embryos (*aqp1a.1*$^{+/rk28}$*;aqp8a.1*$^{+/rk29}$: n = 21 embryos;
725 *aqp1a.1*$^{rk28/rk28}$: n = 20 embryos; *aqp8a.1*$^{rk29/rk29}$: n = 20 embryos; *aqp1a.1*$^{rk28/rk28}$*;aqp8a.1*$^{rk29/rk29}$:
726 n = 19 embryos from 2 independent experiments).
727 (F) Illustration of aISV and vISV connections in the trunk of wild type embryo at 3 dpf.
728 (G-J) Representative maximum intensity projection confocal z-stacks of 3 dpf wild type (G),
729 *aqp8a.1*$^{rk29/rk29}$ (H), *aqp1a.1*$^{rk28/rk28}$ (I), and *aqp1a.1*$^{rk28/rk28}$*;aqp8a.1*$^{rk29/rk29}$ (J) embryos. Asterisk
730 marks incomplete ISVs.
731 (K) Quantification of percentage of wild type and *aquaporin* mutant embryos at 3 dpf with at least
732 one incomplete ISVs per embryo (wild type, n = 47 embryos; *aqp1a.1*$^{rk28/rk28}$, n = 30 embryos;
733 *aqp8a.1*$^{rk29/rk29}$, n = 38 embryos; *aqp1a.1*$^{rk28/rk28}$*;aqp8a.1*$^{rk29/rk29}$, n = 204 embryos).
734 (L) A pie chart showing proportion of different classes of incomplete ISV phenotypes (I-VI) found
735 in *aqp1a.1*$^{rk28/rk28}$*;aqp8a.1*$^{rk29/rk29}$ mutant embryos at 3 dpf.
736 DA, dorsal aorta; DLAV, dorsal longitudinal anastomotic vessel; ISV, intersegmental vessel; aISV,
737 arterial ISV; vISV, venous ISV; NC, notochord; NT, neural tube; PCV, posterior cardinal vein.
738 Scale bar, 50 µm (G-J) and 200 µm (A-D).
739 See also Fig. S6, S7 and S8.
740
741 **Figure 4. Aquaporins promote endothelial tip cell protrusion and migration.**

742 (A) Timing of tip cell emergence from the DA in *aqp1a.1*$^{+/rk28}$*;aqp8a.1*$^{+/rk29}$ (n = 23) and
743 *aqp1a.1*$^{rk28/rk28}$*;aqp8a.1*$^{rk29/rk29}$ (n = 27).
744 (B and C) Still images from time-lapse imaging of migrating tip cells from
745 *aqp1a.1*$^{+/rk28}$*;aqp8a.1*$^{+/rk29}$ (B) and *aqp1a.1*$^{rk28/rk28}$*;aqp8a.1*$^{rk29/rk29}$ (C) embryos from 20 to 30 hpf.
746 White arrows, retracting tip cell. *, secondary sprouting from PCV. Scale bar, 10 µm.
747 (D and E) Stills images from representative time-lapse movies of migrating tip cells in
748 *aqp1a.1*$^{+/rk28}$*;aqp8a.1*$^{+/rk29}$ (D, n = 2) and *aqp1a.1*$^{rk28/rk28}$*;aqp8a.1*$^{rk29/rk29}$ (E, n = 5) embryos.
749 Movies were taken from 25 to 30 hpf (n = 2 independent experiments). Bracket, formation of stable
750 protrusions. Scale bar, 20 µm.
751 (F and G) Representative maximum intensity projection confocal z-stacks of tip cells from wild
752 type (F) and *aqp1a.1*$^{rk28/rk28}$*;aqp8a.1*$^{rk29/rk29}$ (G) embryos at 26 hpf. Scale bar, 10 µm.
753 (H) Quantification of filopodia number in tip cells of wild type (n = 36 cells from 10 embryos, 2
754 independent experiments), *aqp1a.1*$^{+/rk28}$*;aqp8a.1*$^{+/rk29}$ (n = 19 cells from 6 embryos, 2 independent
755 experiments) and *aqp1a.1*$^{rk28/rk28}$*;aqp8a.1*$^{rk29/rk29}$ (n = 28 cells from 9 embryos, 2 independent
756 experiments) embryos.
757 (I) Quantification of filopodia length in tip cells of wild type (n = 24 cells from 7 embryos, 2
758 independent experiments), *aqp1a.1*$^{+/rk28}$*;aqp8a.1*$^{+/rk29}$ (n = 16 cells from 7 embryos, 2 independent
759 experiments) and *aqp1a.1*$^{rk28/rk28}$*;aqp8a.1*$^{rk29/rk29}$ (n = 11 cells from 6 embryos, 2 independent
760 experiments) embryos.
761 (J) Quantification of tip cell leading edge displacement of *aqp1a.1*$^{+/rk28}$*;aqp8a.1*$^{+/rk29}$ (n = 19 cells
762 from 5 embryos, 3 independent experiments) and *aqp1a.1*$^{rk28/rk28}$*;aqp8a.1*$^{rk29/rk29}$ (n = 47 cells from
763 13 embryos, 6 independent experiments) embryos at 25 - 30 hpf.
764 (K) Quantification of tip cell nuclei displacement of *aqp1a.1*$^{+/rk28}$*;aqp8a.1*$^{+/rk29}$ (n = 20 cells from
765 6 embryos, 4 independent experiments) and *aqp1a.1*$^{rk28/rk28}$*;aqp8a.1*$^{rk29/rk29}$ (n = 20 cells from 4
766 embryos, 2 independent experiments) embryos at 21 - 30 hpf.
767 (L) Quantification of tip cell migration velocity in *aqp1a.1*$^{+/rk28}$*;aqp8a.1*$^{+/rk29}$ (n = 19 cells from 5
768 embryos, 3 independent experiments) and *aqp1a.1*$^{rk28/rk28}$*;aqp8a.1*$^{rk29/rk29}$ (n = 47 cells from 13
769 embryos, 6 independent experiments) embryos at 25 - 30 hpf.
770 Statistical significance was determined by Brown-Forsythe and Welch ANOVA tests with
771 Dunnett's (H) or Sidak's (I) multiple comparisons test, and with unpaired *t*-test (L). ns, $p>0.05$, *,
772 $p < 0.05$, ***, $p < 0.001$, and ****, $p < 0.0001$.

773 See also Movie S3-6.

774

775 **Figure 5. Aquaporin-mediated water influx increases tip cell volume and actin elongation in**
776 **filopodia.**

777 (A and B) Representative maximum intensity projection confocal z-stacks of tip cell and its 3D-
778 volume rendering of 25 hpf wild type (A) and *aqp1a.1*$^{rk28/rk28}$*;aqp8a.1*$^{rk29/rk29}$ (B) labelled with
779 cytosolic mEmerald. Scale bar, 10 µm.

780 (C) Quantification of tip cell volume in 25 hpf wild type (n = 24 cells) and
781 *aqp1a.1*$^{rk28/rk28}$*;aqp8a.1*$^{rk29/rk29}$ (n = 20 cells) embryos from 3 independent experiments.

782 (D) Quantification of growth rate of actin bundles in tip cell filopodia in 25 hpf wild type (n = 12
783 cells from 7 embryos, 2 independent experiments) and *aqp1a.1*^{rk28}*;aqp8a.1*^{rk29} (n = 12 cells from
784 6 embryos, 2 independent experiments) embryos.

785 Statistical significance was determined by unpaired *t*-test with (C) or without (D) Welch's
786 correction.

787

788 **Figure 6. Additive function of actin polymerization and hydrostatic pressure in driving EC**
789 **migration and sprouting angiogenesis.**

790 (A-D) Representative maximum intensity projection confocal z-stacks of 28 hpf wild type (A and
791 B) and *aqp1a.1*$^{rk28/rk28}$*;aqp8a.1*$^{rk29/rk29}$ (C and D) embryos treated with 0.1% DMSO (A and C) or
792 0.8 µg/ml Lat. B (B and D) from 20 to 28 hpf (for each condition: wild type, n = 10 embryos;
793 *aqp1a.1*$^{rk28/rk28}$*;aqp8a.1*$^{rk29/rk29}$, n =12 embryos, 2 independent experiments). Scale bar, 20 µm.

794 (E) Quantification of ISV length in 28 hpf wild type and *aqp1a.1*$^{rk28/rk28}$*;aqp8a.1*$^{rk29/rk29}$ embryos
795 treated with 0.1% DMSO or 0.8 µg/ml Lat. B (wild type: n = 60 vessels from 10 control embryos,
796 n = 66 vessels from 10 Lat. B-treated embryos; *aqp1a.1*^{rk28}*;aqp8a.1*^{rk29}: n = 126 vessels from 12
797 control embryos, n = 112 vessels from 11 Lat. B-treated embryos, 2 independent experiments).
798 Statistical significance was determined by Brown-Forsythe ANOVA test with Sidak's multiple
799 comparison test; ns, *p*,>,0.05, **,$p < 0.01$, and ****, $p < 0.0001$. (F) Endothelial tip cells generate
800 membrane protrusions by actin polymerization and increased hydrostatic pressure via Aquaporin-
801 mediated water inflow. In the absence of actin polymerization and presence of Aquaporins,
802 hydrostatic pressure deforms membranes to generate membrane protrusions. When Aquaporin

803 function is lost, membrane protrusions is generated by actin polymerization. Fewer membrane
804 protrusions are formed when only one mechanism is utilized, resulting in slower EC migration.
805 See also Movie S7.
806
807 **References**
808

809 Agre P, King LS, Yasui M, Guggino WB, Ottersen OP, Fujiyoshi Y, Engel A, Nielsen S. 2002.
810 Aquaporin water channels – from atomic structure to clinical medicine. *J Physiol* **542**:3–16.
811 doi:10.1113/jphysiol.2002.020818

812 Ando K, Wang W, Peng D, Chiba A, Lagendijk AK, Barske L, Crump JG, Stainier DYR,
813 Lendahl U, Koltowska K, Hogan BM, Fukuhara S, Mochizuki N, Betsholtz C. 2019. Peri-
814 arterial specification of vascular mural cells from naïve mesenchyme requires Notch
815 signaling. *Development* **146**:dev165589-13. doi:10.1242/dev.165589

816 Baeyens N, Nicoli S, Coon BG, Ross TD, Dries K den, Han J, Lauridsen HM, Mejean CO,
817 Eichmann A, Thomas J-L, Humphrey JD, Schwartz MA. 2015. Vascular remodeling is
818 governed by a VEGFR3-dependent fluid shear stress set point. *Elife* **4**.
819 doi:10.7554/elife.04645

820 Benedito R, Hellström M. 2013. Notch as a hub for signaling in angiogenesis. *Exp Cell Res* 1–8.

821 Benfenati V, Caprini M, Dovizio M, Mylonakou MN, Ferroni S, Ottersen OP, Amiry-
822 Moghaddam M. 2011. An aquaporin-4/transient receptor potential vanilloid 4
823 (AQP4/TRPV4) complex is essential for cell-volume control in astrocytes. *Proc Natl Acad*
824 *Sci USA* **108**:2563–8. doi:10.1073/pnas.1012867108

825 Bill BR, Korzh V. 2014. Choroid plexus in developmental and evolutionary perspective. *Front*
826 *Neurosci* **8**:363. doi:10.3389/fnins.2014.00363

827 Boer LL de, Vanes L, Melgrati S, O'May JB, Hayward D, Driscoll PC, Day J, Griffiths A,
828 Magueta R, Morrell A, MacRae JI, Köchl R, Tybulewicz VLJ. 2023. T cell migration requires
829 ion and water influx to regulate actin polymerization. *Nat Commun* **14**:7844.
830 doi:10.1038/s41467-023-43423-8

831 Bussmann J, Wolfe SA, Siekmann AF. 2011. Arterial-venous network formation during brain
832 vascularization involves hemodynamic regulation of chemokine signaling. *Development*
833 **138**:1717–1726.

834 Calamita G, Ferri D, Gena P, Liquori GE, Cavalier A, Thomas D, Svelto M. 2005. The Inner
835 Mitochondrial Membrane Has Aquaporin-8 Water Channels and Is Highly Permeable to
836 Water. *J Biol Chem* **280**:17149–17153. doi:10.1074/jbc.c400595200

837 Chae YK, Woo J, Kim M-J, Kang SK, Kim MS, Lee J, Lee SK, Gong G, Kim YH, Soria JC,
838 Jang SJ, Sidransky D, Moon C. 2008. Expression of Aquaporin 5 (AQP5) Promotes Tumor
839 Invasion in Human Non Small Cell Lung Cancer. *PLoS ONE* **3**:e2162.
840 doi:10.1371/journal.pone.0002162

841 Chan CJ, Costanzo M, Ruiz-Herrero T, Mönke G, Petrie RJ, Bergert M, Diz-Muñoz A,
842 Mahadevan L, Hiiragi T. 2019. Hydraulic control of mammalian embryo size and cell fate.
843 *Nature* **571**:112–116. doi:10.1038/s41586-019-1309-x

844 Chang Y-F, Imam JS, Wilkinson MF. 2007. The Nonsense-Mediated Decay RNA Surveillance
845 Pathway. *Annu Rev Biochem* **76**:51–74. doi:10.1146/annurev.biochem.76.050106.093909

846 Chauvigné F, Boj M, Finn RN, Cerdà J. 2015. Mitochondrial aquaporin-8-mediated hydrogen
847 peroxide transport is essential for teleost spermatozoon motility. *Sci Rep* **5**:7789.
848 doi:10.1038/srep07789

849 Chauvigné F, Ducat C, Ferré A, Hansen T, Carrascal M, Abián J, Finn RN, Cerdà J. 2021. A
850 multiplier peroxiporin signal transduction pathway powers piscine spermatozoa. *Proc Natl*
851 *Acad Sci USA* **118**:e2019346118. doi:10.1073/pnas.2019346118

852 Choudhury MI, Benson MA, Sun SX. 2022. Trans-epithelial fluid flow and mechanics of
853 epithelial morphogenesis. *Semin Cell Dev Biol* **131**:146–159.
854 doi:10.1016/j.semcdb.2022.05.020

855 Chugh M, Munjal A, Megason SG. 2022. Hydrostatic pressure as a driver of cell and tissue
856 morphogenesis. *Semin Cell Dev Biol* **131**:134–145. doi:10.1016/j.semcdb.2022.04.021

857 Clarke DN, Martin AC. 2021. Actin-based force generation and cell adhesion in tissue
858 morphogenesis. *Curr Biol* **31**:R667–R680. doi:10.1016/j.cub.2021.03.031

859 Conner MT, Conner AC, Bland CE, Taylor LHJ, Brown JEP, Parri HR, Bill RM. 2012. Rapid
860 Aquaporin Translocation Regulates Cellular Water Flow. *J Biol Chem* **287**:11516–11525.
861 doi:10.1074/jbc.m111.329219

862 Day RE, Kitchen P, Owen DS, Bland C, Marshall L, Conner AC, Bill RM, Conner MT. 2014.
863 Human aquaporins: regulators of transcellular water flow. *Biochim Biophys Acta* **1840**:1492–
864 1506. doi:10.1016/j.bbagen.2013.09.033

865 Dumortier JG, Verge-Serandour ML, Tortorelli AF, Mielke A, Plater L de, Turlier H, Maître J-L.
866 2019. Hydraulic fracturing and active coarsening position the lumen of the mouse blastocyst.
867 *Science* **365**:465–468. doi:10.1126/science.aaw7709

868 Emelyanov A, Gao Y, Naqvi NI, Parinov S. 2006. Trans-Kingdom Transposition of the Maize
869 Dissociation Element. *Genetics* **174**:1095–1104. doi:10.1534/genetics.106.061184

870 Emelyanov A, Parinov S. 2008. Mifepristone-inducible LexPR system to drive and control gene
871 expression in transgenic zebrafish. *Dev Biol* **320**:113–121. doi:10.1016/j.ydbio.2008.04.042

872 Farinas J, Kneen M, Moore M, Verkman AS. 1997. Plasma Membrane Water Permeability of
873 Cultured Cells and Epithelia Measured by Light Microscopy with Spatial Filtering. *J Gen*
874 *Physiol* **110**:283–296. doi:10.1085/jgp.110.3.283

875 Figueiredo AM, Barbacena P, Russo A, Vaccaro S, Ramalho D, Pena A, Lima AP, Ferreira RR,
876 Fidalgo MA, El-Marjou F, Carvalho Y, Vasconcelos FF, Lennon-Duménil A-M, Vignjevic
877 DM, Franco CA. 2021. Endothelial cell invasion is controlled by dactylopodia. *Proc Natl*
878 *Acad Sci USA* **118**. doi:10.1073/pnas.2023829118

879 Fukuhara S, Zhang J, Yuge S, Ando K, Wakayama Y, Sakaue-Sawano A, Miyawaki A,
880 Mochizuki N. 2014. Visualizing the cell-cycle progression of endothelial cells in zebrafish.
881 *Dev Biol* **393**:10–23. doi:10.1016/j.ydbio.2014.06.015

882 Gagnon JA, Valen E, Thyme SB, Huang P, Akhmetova L, Ahkmetova L, Pauli A, Montague
883 TG, Zimmerman S, Richter C, Schier AF. 2014. Efficient mutagenesis by Cas9 protein-
884 mediated oligonucleotide insertion and large-scale assessment of single-guide RNAs. *PLoS*
885 *ONE* **9**:e98186. doi:10.1371/journal.pone.0098186

886 Gebala V, Collins R, Geudens I, Phng L-K, Gerhardt H. 2016. Blood flow drives lumen
887 formation by inverse membrane blebbing during angiogenesis in vivo. *Nat Cell Biol* **18**:443–
888 450. doi:10.1038/ncb3320

889 Gerhardt H, Golding M, Fruttiger M, Ruhrberg C, Lundkvist A, Abramsson A, Jeltsch M,
890 Mitchell C, Alitalo K, Shima D, Betsholtz C. 2003. VEGF guides angiogenic sprouting
891 utilizing endothelial tip cell filopodia. *J Cell Biol* **161**. doi:10.1083/jcb.200302047

892 Gradilone SA, Carreras FI, Lehmann GL, Marinelli RA. 2005. Phosphoinositide 3-kinase is
893 involved in the glucagon-induced translocation of aquaporin-8 to hepatocyte plasma
894 membrane. *Biol Cell* **97**:831–836. doi:10.1042/bc20040115

895 Gradilone SA, García F, Huebert RC, Tietz PS, Larocca MC, Kierbel A, Carreras FI, Larusso
896 NF, Marinelli RA. 2003. Glucagon induces the plasma membrane insertion of functional
897 aquaporin-8 water channels in isolated rat hepatocytes. *Hepatology* **37**:1435–41.
898 doi:10.1053/jhep.2003.50241

899 Gross-Thebing T, Paksa A, Raz E. 2014. Simultaneous high-resolution detection of multiple
900 transcripts combined with localization of proteins in whole-mount embryos. *BMC Biol* **12**:55.
901 doi:10.1186/s12915-014-0055-7

902 Groth C, Alvord WG, Quiñones OA, Fortini ME. 2010. Pharmacological Analysis of Drosophila
903 melanogaster γ-Secretase with Respect to Differential Proteolysis of Notch and APP. *Mol*
904 *Pharmacol* **77**:567–574. doi:10.1124/mol.109.062471

905 Herrera M, Garvin JL. 2007. Novel role of AQP-1 in NO-dependent vasorelaxation. *Am J*
906 *Physiol Ren Physiol* **292**:F1443–F1451. doi:10.1152/ajprenal.00353.2006

907 Herrera M, Hong NJ, Garvin JL. 2006. Aquaporin-1 Transports NO Across Cell Membranes.
908 *Hypertension* **48**:157–164. doi:10.1161/01.hyp.0000223652.29338.77

909 Hogan BM, Bos FL, Bussmann J, Witte M, Chi NC, Duckers HJ, Schulte-Merker S. 2009. ccbe1
910 is required for embryonic lymphangiogenesis and venous sprouting. *Nat Genet* **41**.
911 doi:10.1038/ng.321

912 Hu J, Verkman AS, Hu J, Verkman AS. 2006. Increased migration and metastatic potential of
913 tumor cells expressing aquaporin water channels. *FASEB J* **20**:1892–1894. doi:10.1096/fj.06-
914 5930fje

915 Jahn TP, Møller ALB, Zeuthen T, Holm LM, Klærke DA, Mohsin B, Kühlbrandt W, Schjoerring
916 JK. 2004. Aquaporin homologues in plants and mammals transport ammonia. *FEBS Lett*
917 **574**:31–36. doi:10.1016/j.febslet.2004.08.004

918 Jin S-W, Beis D, Mitchell T, Chen J-N, Stainier DY. 2005. Cellular and molecular analyses of
919 vascular tube and lumen formation in zebrafish. *Development* **132**. doi:10.1242/dev.02087

920 Jung HJ, Park J-Y, Jeon H-S, Kwon T-H. 2011. Aquaporin-5: A Marker Protein for Proliferation
921 and Migration of Human Breast Cancer Cells. *PLoS ONE* **6**:e28492.
922 doi:10.1371/journal.pone.0028492

923 Karlsson T, Bolshakova A, Magalhães MAO, Loitto VM, Magnusson K-E. 2013. Fluxes of
924 Water through Aquaporin 9 Weaken Membrane-Cytoskeleton Anchorage and Promote
925 Formation of Membrane Protrusions. *PLoS ONE* **8**:e59901.
926 doi:10.1371/journal.pone.0059901

927 Karlsson T, Glogauer M, Ellen RP, Loitto V, Magnusson K, Magalhães MAO. 2011. Aquaporin
928 9 phosphorylation mediates membrane localization and neutrophil polarization. *J Leukoc Biol*
929 **90**:963–973. doi:10.1189/jlb.0910540

930 Kimmel CB, Ballard WW, Kimmel SR, Ullmann B, Schilling TF. 1995. Stages of embryonic
931 development of the zebrafish. *Dev Dyn* **203**:253--310.

932 Kondrychyn I, Kelly DJ, Carretero NT, Nomori A, Kato K, Chong J, Nakajima H, Okuda S,
933 Mochizuki N, Phng L-K. 2020. Marcksl1 modulates endothelial cell mechanoresponse to
934 haemodynamic forces to control blood vessel shape and size. *Nat Commun* **11**:5476–18.
935 doi:10.1038/s41467-020-19308-5

936 Koun S, Kim J-D, Rhee M, Kim M-J, Huh T-L. 2016. Spatiotemporal expression pattern of the
937 zebrafish aquaporin 8 family during early developmental stages. *Gene Expr Patterns* **21**:1–6.
938 doi:10.1016/j.gep.2016.06.001

939 Kozono D, Yasui M, King LS, Agre P. 2002. Aquaporin water channels: atomic structure
940 molecular dynamics meet clinical medicine. *J Clin Invest* **109**:1395–1399.
941 doi:10.1172/jci15851

942 Li Y, Konstantopoulos K, Zhao R, Mori Y, Sun SX. 2020. The importance of water and
943 hydraulic pressure in cell dynamics. *J Cell Sci* **133**:jcs240341. doi:10.1242/jcs.240341

944 Liu K, Nagase H, Huang CG, Calamita G, Agre P. 2006. Purification and functional
945 characterization of aquaporin-8. *Biol Cell* **98**:153–161. doi:10.1042/bc20050026

946 Loitto VM, Huang C, Sigal YJ, Jacobson K. 2007. Filopodia are induced by aquaporin-9
947 expression. *Exp Cell Res* **313**:1295–1306. doi:10.1016/j.yexcr.2007.01.023

948 Loitto VM, Karlsson T, Magnusson K. 2009. Water flux in cell motility: Expanding the
949 mechanisms of membrane protrusion. *Cell Motil Cytoskeleton* **66**:237–247.
950 doi:10.1002/cm.20357

951 Ma T, Yang B, Verkman AS. 1997. Cloning of a Novel Water and Urea-Permeable Aquaporin
952 from Mouse Expressed Strongly in Colon, Placenta, Liver, and Heart. *Biochem Biophys Res*
953 *Commun* **240**:324–328. doi:10.1006/bbrc.1997.7664

954 Mallavarapu A, Mitchison T. 1999. Regulated Actin Cytoskeleton Assembly at Filopodium Tips
955 Controls Their Extension and Retraction. *J Cell Biol* **146**:1097–1106.
956 doi:10.1083/jcb.146.5.1097

957 Maltaneri RE, Schiappacasse A, Chamorro ME, Nesse AB, Vittori DC. 2020. Aquaporin-1 plays
958 a key role in erythropoietin-induced endothelial cell migration. *Biochim Biophys Acta Mol*
959 *Cell Res* **1867**:118569. doi:10.1016/j.bbamcr.2019.118569

960 Marikawa Y, Alarcon VB. 2012. Mouse Development, From Oocyte to Stem Cells. *Results*
961 *Probl Cell Differ* **55**:165–184. doi:10.1007/978-3-642-30406-4_9

962 Markou A, Unger L, Abir-Awan M, Saadallah A, Halsey A, Balklava Z, Conner M, Törnroth-
963 Horsefield S, Greenhill SD, Conner A, Bill RM, Salman MM, Kitchen P. 2022. Molecular
964 mechanisms governing aquaporin relocalisation. *Biochim Biophys Acta Biomembr*
965 **1864**:183853. doi:10.1016/j.bbamem.2021.183853

966 McLennan R, McKinney MC, Teddy JM, Morrison JA, Kasemeier-Kulesa JC, Ridenour DA,
967 Manthe CA, Giniunaite R, Robinson M, Baker RE, Maini PK, Kulesa PM. 2019. Neural crest
968 cells bulldoze through the microenvironment using Aquaporin 1 to stabilize filopodia.
969 *Development* **147**:dev185231. doi:10.1242/dev.185231

970 Meeker ND, Hutchinson SA, Ho L, Trede NS. 2007. Method for isolation of PCR-ready
971 genomic DNA from zebrafish tissues. *Biotech* **43**:610–614.

972 Mosaliganti KR, Swinburne IA, Chan CU, Obholzer ND, Green AA, Tanksale S, Mahadevan L,
973 Megason SG. 2019. Size control of the inner ear via hydraulic feedback. *Elife* **8**:e39596.
974 doi:10.7554/elife.39596

975 Munjal A, Lecuit T. 2014. Actomyosin networks and tissue morphogenesis. *Development*
976 **141**:1789-1793. doi:10.1242/dev.091645

977 Murrell M, Oakes PW, Lenz M, Gardel ML. 2015. Forcing cells into shape: the mechanics of
978 actomyosin contractility. *Nat Cell Biol* **16**:486–498. doi:10.1038/nrm4012

979 Nagy TL, Strickland J, Weiner OD. 2023. Neutrophils actively swell to potentiate rapid
980 migration. *bioRxiv* 2023.05.15.540704. doi:10.1101/2023.05.15.540704

981 Nakajima H, Yamamoto K, Agarwala S, Terai K, Fukui H, Fukuhara S, Ando K, Miyazaki T,
982 Yokota Y, Schmelzer E, Belting H-G, Affolter M, Lecaudey V, Mochizuki N. 2017. Flow-
983 Dependent Endothelial YAP Regulation Contributes to Vessel Maintenance. *Dev Cell* **40**:523-
984 536.e6. doi:10.1016/j.devcel.2017.02.019

985 Nakhoul NL, Davis BA, Romero MF, Boron WF. 1998. Effect of expressing the water channel
986 aquaporin-1 on the CO2 permeability of Xenopus oocytes. *Am J Physiol Cell Physiol*
987 **274**:C543–C548. doi:10.1152/ajpcell.1998.274.2.c543

988 Noda Y, Sasaki S. 2005. Trafficking mechanism of water channel aquaporin-2. *Biol Cell*
989 **97**:885–892. doi:10.1042/bc20040120

990 Papadopoulos MC, Saadoun S, Verkman AS. 2008. Aquaporins and cell migration. *Pflugers*
991 *Arch* **456**:693–700. doi:10.1007/s00424-007-0357-5

992 Parab S, Quick RE, Matsuoka RL. 2021. Endothelial cell-type-specific molecular requirements
993 for angiogenesis drive fenestrated vessel development in the brain. *Elife* **10**:e64295.
994 doi:10.7554/elife.64295

995 Pfaffl MW. 2001. A new mathematical model for relative quantification in real-time RT–PCR.
996 *Nucleic Acids Res* **29**:e45–e45. doi:10.1093/nar/29.9.e45

997 Phng LK, Gerhardt H. 2009. Angiogenesis: A Team Effort Coordinated by Notch. *Dev Cell*
998 **16**:196–208. doi:10.1016/j.devcel.2009.01.015

999 Phng LK, Stanchi F, Gerhardt H. 2013. Filopodia are dispensable for endothelial tip cell
1000 guidance. *Development* **140**:4031--4040.

1001 Phng L-K, Stanchi F, Gerhardt H. 2013. Filopodia are dispensable for endothelial tip cell
1002 guidance. *Development* **140**:4031–4040. doi:10.1242/dev.097352

1003 Prasad GV, Coury LA, Finn F, Zeidel ML. 1998. Reconstituted aquaporin 1 water channels
1004 transport CO2 across membranes. *J Biol Chem* **273**:33123–6. doi:10.1074/jbc.273.50.33123

1005 Preston GM, Carroll TP, Guggino WB, Agre P. 1992. Appearance of water channels in Xenopus
1006 oocytes expressing red cell CHIP28 protein. *Science* **256**:385–7.
1007 doi:10.1126/science.256.5055.385

1008 Rehn K, Wong KS, Balciunas D, Sumanas S. 2011. Zebrafish enhancer trap line recapitulates
1009 embryonic aquaporin 1a expression pattern in vascular endothelial cells. *Int J Dev Biol*
1010 **55**:613–618. doi:10.1387/ijdb.103249kp

1011 Ridley AJ. 2011. Life at the Leading Edge. *Cell* **145**:1012–1022. doi:10.1016/j.cell.2011.06.010

1012 Saadoun S, Papadopoulos MC, Hara-Chikuma M, Verkman AS. 2005. Impairment of
1013 angiogenesis and cell migration by targeted aquaporin-1 gene disruption. *Nature* **434**:786–
1014 792. doi:10.1038/nature03460

1015 Sato Y, Shigematsu M, Shibata-Kanno M, Maejima S, Tamura C, Sakamoto H. 2023. Aquaporin
1016 regulates cell rounding through vacuole formation during endothelial-to-hematopoietic
1017 transition. *Development* **150**. doi:10.1242/dev.201275

1018 Sauteur L, Affolter M, Belting H-G. 2017. Distinct and redundant functions of Esama and VE-
1019 cadherin during vascular morphogenesis. *Development* **144**:1554–1565.
1020 doi:10.1242/dev.140038

1021 Siekmann AF, Affolter M, Belting H-G. 2013. The tip cell concept 10 years after: New players
1022 tune in for a common theme. *Exp Cell Res* **319**:1255–1263.

1023 Son S, Kang JH, Oh S, Kirschner MW, Mitchison TJ, Manalis S. 2015. Resonant microchannel
1024 volume and mass measurements show that suspended cells swell during mitosis. *J Cell Biol*
1025 **211**:757–763. doi:10.1083/jcb.201505058

1026 Soria LR, Fanelli E, Altamura N, Svelto M, Marinelli RA, Calamita G. 2010. Aquaporin-8-
1027 facilitated mitochondrial ammonia transport. *Biochem Biophys Res Commun* **393**:217–221.
1028 doi:10.1016/j.bbrc.2010.01.104

1029 Stewart MP, Helenius J, Toyoda Y, Ramanathan SP, Muller DJ, Hyman AA. 2011. Hydrostatic
1030 pressure and the actomyosin cortex drive mitotic cell rounding. *Nature* **469**:226–230.
1031 doi:10.1038/nature09642

1032 Stroka KM, Jiang H, Chen S-H, Tong Z, Wirtz D, Sun SX, Konstantopoulos K. 2014. Water
1033 permeation drives tumor cell migration in confined microenvironments. *Cell* **157**:611–623.
1034 doi:10.1016/j.cell.2014.02.052

1035 Talbot K, Kwong RWM, Gilmour KM, Perry SF. 2015. The water channel aquaporin-1a1
1036 facilitates movement of CO2 and ammonia in zebrafish (Danio rerio) larvae. *J Exp Biol*
1037 **218**:3931–3940. doi:10.1242/jeb.129759

1038 Thisse C, Thisse B. 2007. High-resolution in situ hybridization to whole-mount zebrafish
1039 embryos. *Nat Protoc* **3**:59–69. doi:10.1038/nprot.2007.514

1040 Tingaud-Sequeira A, Calusinska M, Finn RN, Chauvigné F, Lozano J, Cerdà J. 2010. The
1041 zebrafish genome encodes the largest vertebrate repertoire of functional aquaporins with dual
1042 paralogy and substrate specificities similar to mammals. *BMC Evol Biol* **10**:38.
1043 doi:10.1186/1471-2148-10-38

1044 Wakayama Y, Fukuhara S, Ando K, Matsuda M, Mochizuki N. 2015. Cdc42 Mediates Bmp-
1045 Induced Sprouting Angiogenesis through Fmnl3-Driven Assembly of Endothelial Filopodia in
1046 Zebrafish. *Dev Cell* **32**:109–122. doi:10.1016/j.devcel.2014.11.024

1047 Wang Y, Cohen J, Boron WF, Schulten K, Tajkhorshid E. 2007. Exploring gas permeability of
1048 cellular membranes and membrane channels with molecular dynamics. *J Struct Biol* **157**:534–
1049 544. doi:10.1016/j.jsb.2006.11.008

1050 Wu DQ, Yang ZF, Wang KJ, Feng XY, Lv ZJ, Li Y, Jian ZX. 2017. AQP8 inhibits colorectal
1051 cancer growth and metastasis by down-regulating PI3K/AKT signaling and PCDH7
1052 expression. *Am J Cancer Res* **8**:266–279.

1053 Zeidel ML, Ambudkar SV, Smith BL, Agre P. 1992. Reconstitution of functional water channels
1054 in liposomes containing purified red cell CHIP28 protein. *Biochemistry* **31**:7436–7440.
1055 doi:10.1021/bi00148a002

1056

Figure 1

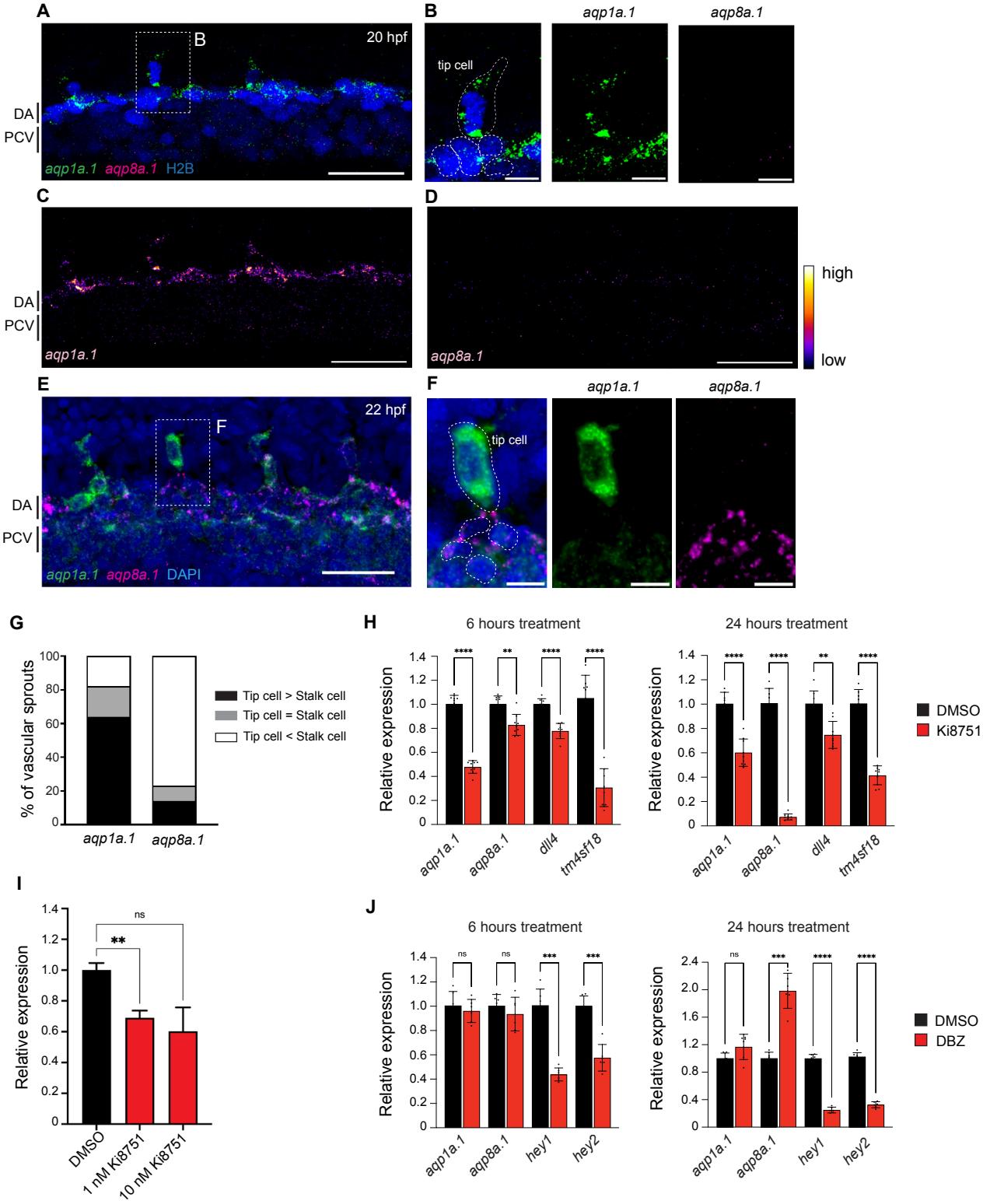
A
20 hpf
B
DA
PCV
aqp1a.1 aqp8a.1 H2B
B
aqp1a.1
aqp8a.1
tip cell
C
DA
PCV
aqp1a.1
D
aqp8a.1
high
low
E
22 hpf
F
DA
PCV
aqp1a.1 aqp8a.1 DAPI
F
aqp1a.1
aqp8a.1
tip cell
G
% of vascular sprouts
Tip cell > Stalk cell
Tip cell = Stalk cell
Tip cell < Stalk cell
aqp1a.1
aqp8a.1
H
6 hours treatment
24 hours treatment
Relative expression
DMSO
Ki8751
aqp1a.1
aqp8a.1
dll4
tm4sf18
I
Relative expression
ns
**
DMSO
1 nM Ki8751
10 nM Ki8751
J
6 hours treatment
24 hours treatment
Relative expression
DMSO
DBZ
aqp1a.1
aqp8a.1
hey1
hey2

Figure 2

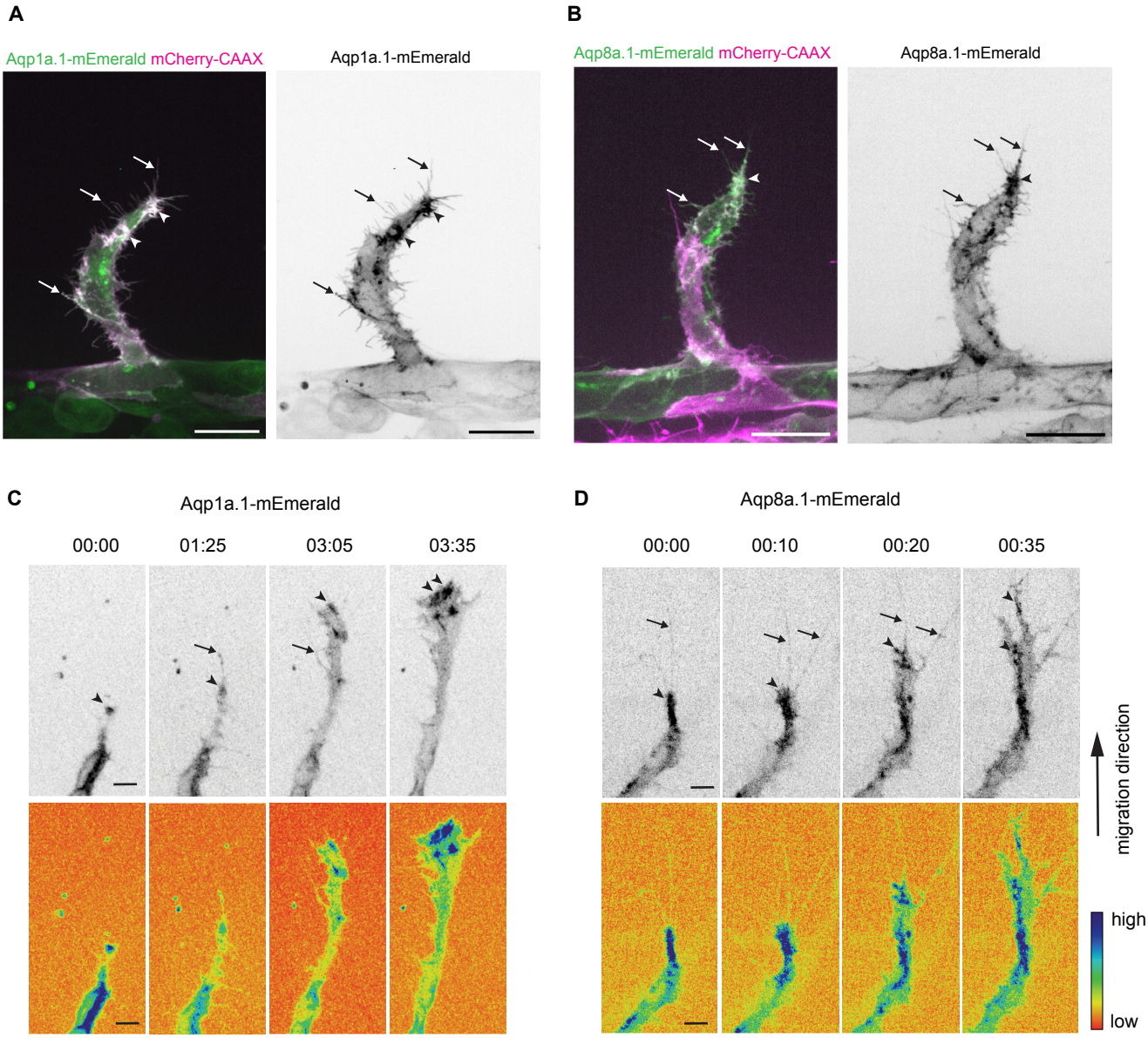
A
Aqp1a.1-mEmerald mCherry-CAAX
Aqp1a.1-mEmerald
B
Aqp8a.1-mEmerald mCherry-CAAX
Aqp8a.1-mEmerald
C
Aqp1a.1-mEmerald
00:00
01:25
03:05
03:35
D
Aqp8a.1-mEmerald
00:00
00:10
00:20
00:35
migration direction
high
low

Figure 3

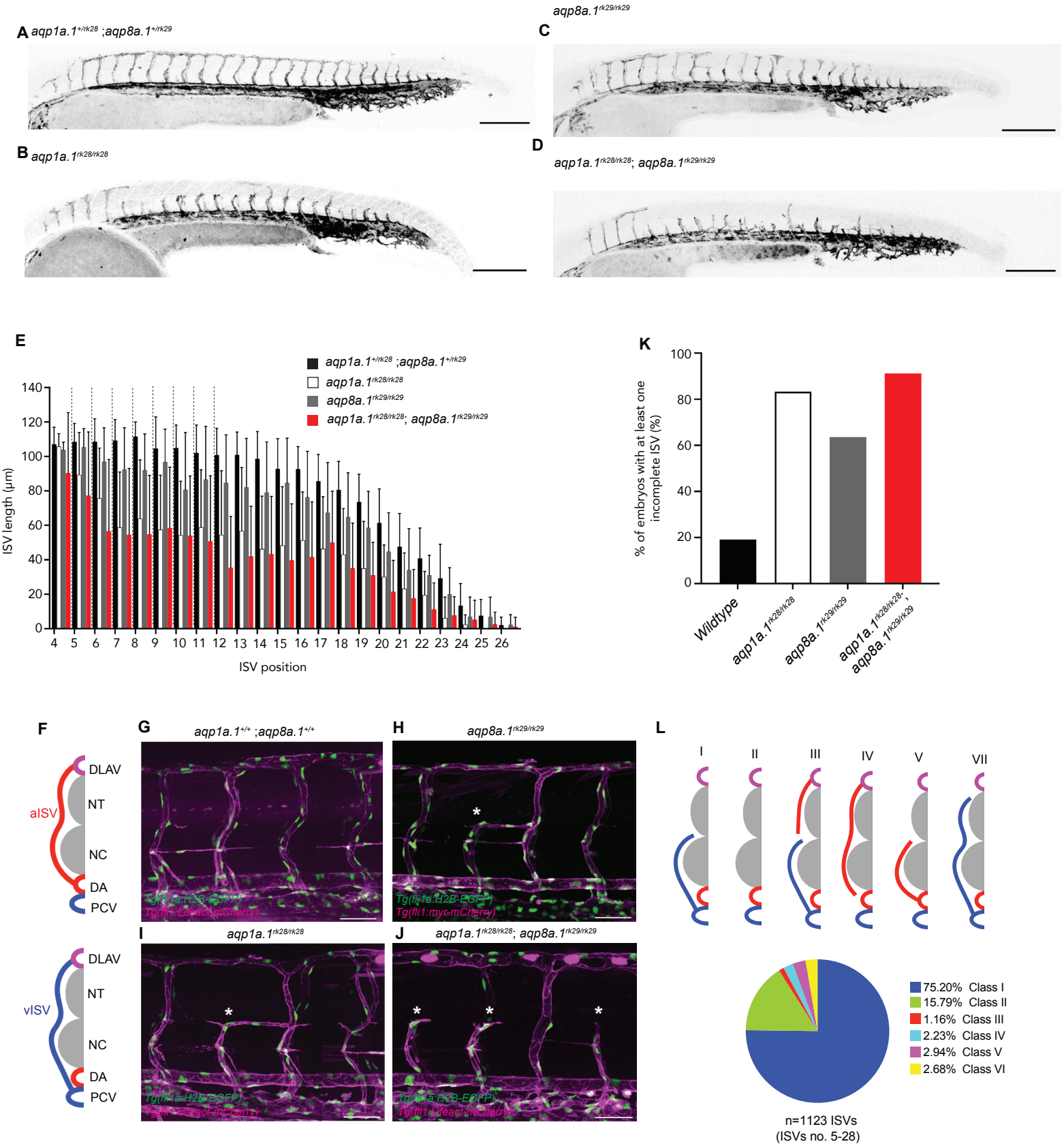
A aqp1a.1+/rk28 ;aqp8a.1+/rk29
B aqp1a.1rk28/rk28
C aqp8a.1rk29/rk29
D aqp1a.1rk28/rk28; aqp8a.1rk29/rk29
E
aqp1a.1+/rk28 ;aqp8a.1+/rk29
aqp1a.1rk28/rk28
aqp8a.1rk29/rk29
aqp1a.1rk28/rk28; aqp8a.1rk29/rk29
ISV length (µm)
ISV position
K
% of embryos with at least one incomplete ISV (%)
Wildtype
aqp1a.1rk28/rk28
aqp8a.1rk29/rk29
aqp1a.1rk28/rk28; aqp8a.1rk29/rk29
F
DLAV
aISV
NT
NC
DA
PCV
vISV
G aqp1a.1+/+ ;aqp8a.1+/+
H aqp8a.1rk29/rk29
I aqp1a.1rk28/rk28
J aqp1a.1rk28/rk28; aqp8a.1rk29/rk29
Tg(fli1a:H2B-EGFP)
Tg(fli1:myr-mCherry)
Tg(fli1:Lifeact-mCherry)
L
I
II
III
IV
V
VII
75.20% Class I
15.79% Class II
1.16% Class III
2.23% Class IV
2.94% Class V
2.68% Class VI
n=1123 ISVs
(ISVs no. 5-28)

Figure 4

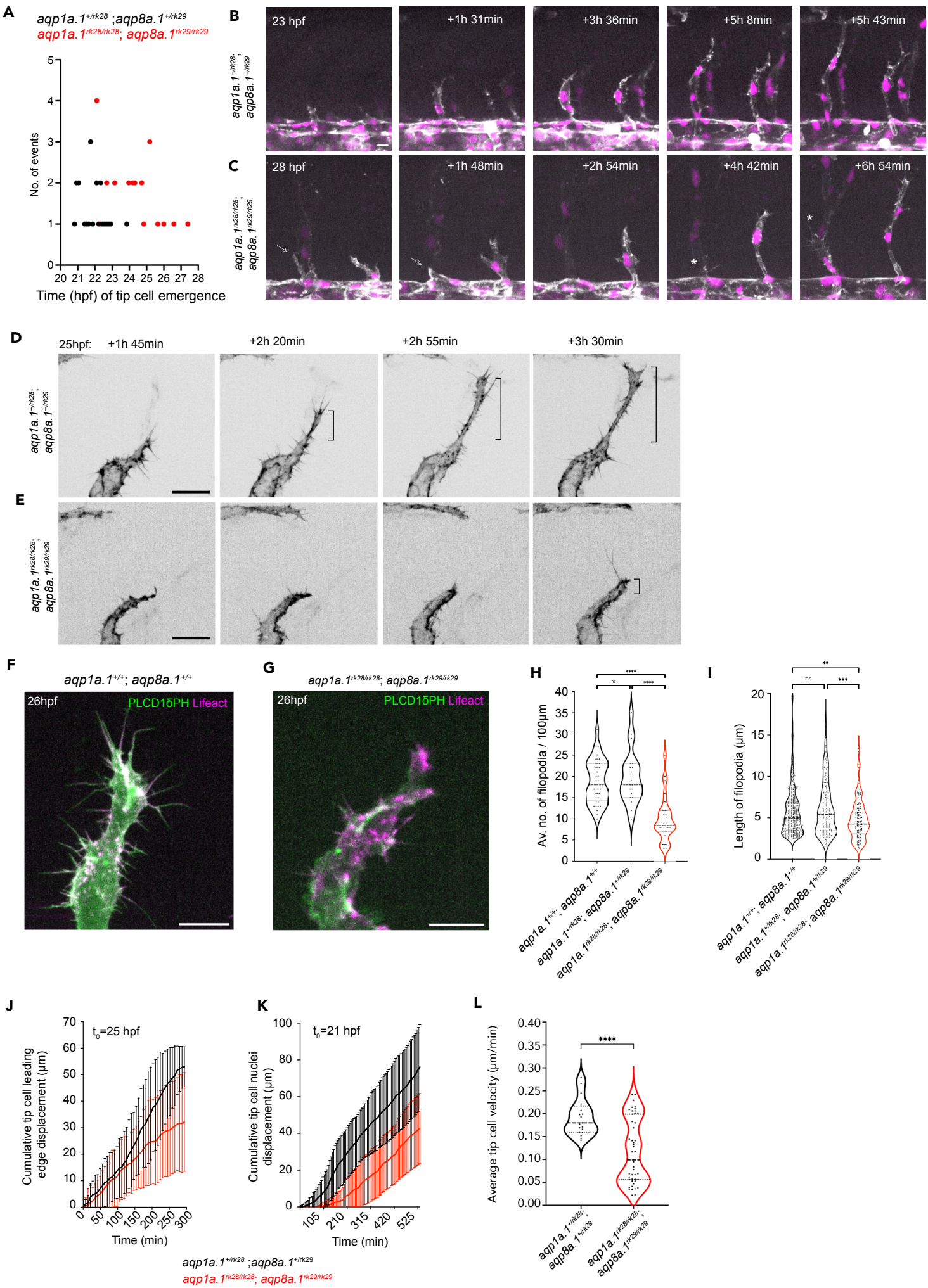
A
aqp1a.1+/rk28 ;aqp8a.1+/rk29
aqp1a.1rk28/rk28; aqp8a.1rk29/rk29
No. of events
Time (hpf) of tip cell emergence
B
aqp1a.1+/rk28; aqp8a.1+/rk29
23 hpf
+1h 31min
+3h 36min
+5h 8min
+5h 43min
C
aqp1a.1rk28/rk28; aqp8a.1rk29/rk29
28 hpf
+1h 48min
+2h 54min
+4h 42min
+6h 54min
D
25hpf: +1h 45min
+2h 20min
+2h 55min
+3h 30min
aqp1a.1+/rk28; aqp8a.1+/rk29
E
aqp1a.1rk28/rk28; aqp8a.1rk29/rk29
F
aqp1a.1+/+; aqp8a.1+/+
26hpf
PLCD1δPH Lifeact
G
aqp1a.1rk28/rk28; aqp8a.1rk29/rk29
26hpf
PLCD1δPH Lifeact
H
Av. no. of filopodia / 100µm
aqp1a.1+/+; aqp8a.1+/+
aqp1a.1+/rk28; aqp8a.1+/rk29
aqp1a.1rk28/rk28; aqp8a.1rk29/rk29
I
Length of filopodia (µm)
aqp1a.1+/+; aqp8a.1+/+
aqp1a.1+/rk28; aqp8a.1+/rk29
aqp1a.1rk28/rk28; aqp8a.1rk29/rk29
J
t0=25 hpf
Cumulative tip cell leading edge displacement (µm)
Time (min)
K
t0=21 hpf
Cumulative tip cell nuclei displacement (µm)
Time (min)
L
Average tip cell velocity (µm/min)
aqp1a.1+/rk28; aqp8a.1+/rk29
aqp1a.1rk28/rk28; aqp8a.1rk29/rk29
aqp1a.1+/rk28 ;aqp8a.1+/rk29
aqp1a.1rk28/rk28; aqp8a.1rk29/rk29

Figure 5

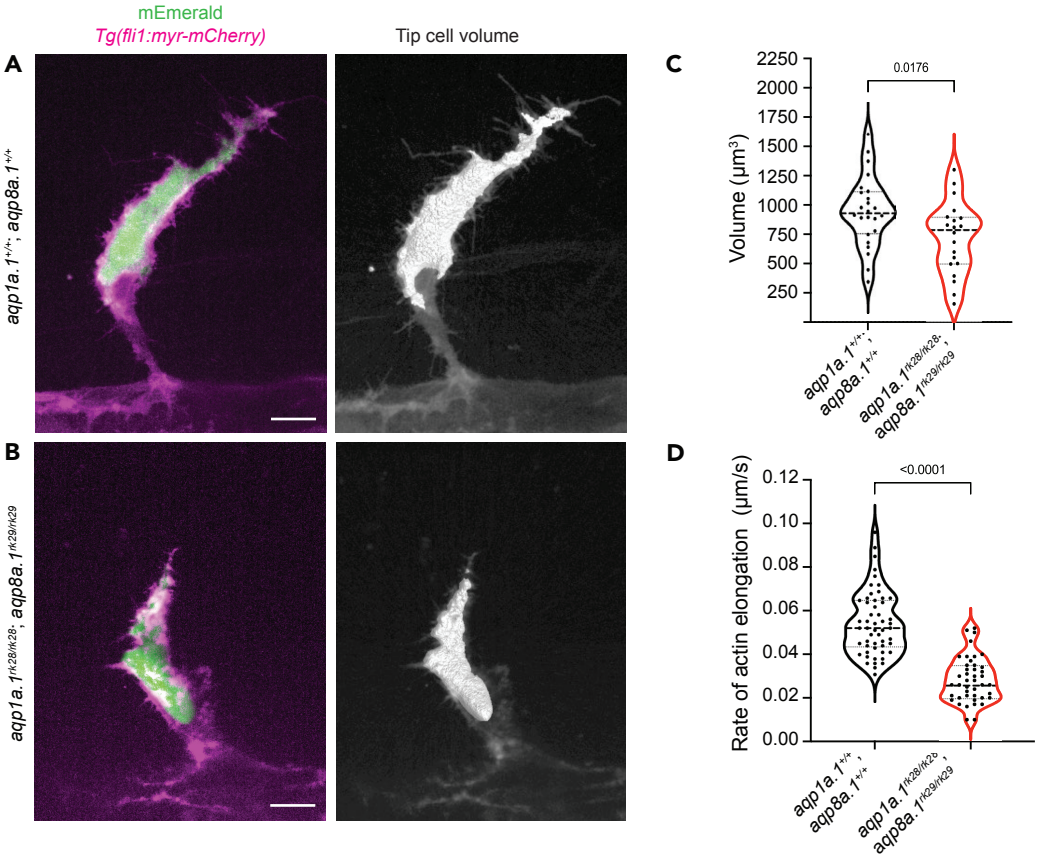
mEmerald
Tg(fli1:myr-mCherry)
Tip cell volume
A
B
C
D
aqp1a.1+/+; aqp8a.1+/+
aqp1a.1rk28/rk28-; aqp8a.1rk29/rk29
Volume (µm3)
0.0176
Rate of actin elongation (µm/s)
<0.0001
aqp1a.1+/+, aqp8a.1+/+
aqp1a.1rk28/rk28-, aqp8a.1rk29/rk29

Figure 6

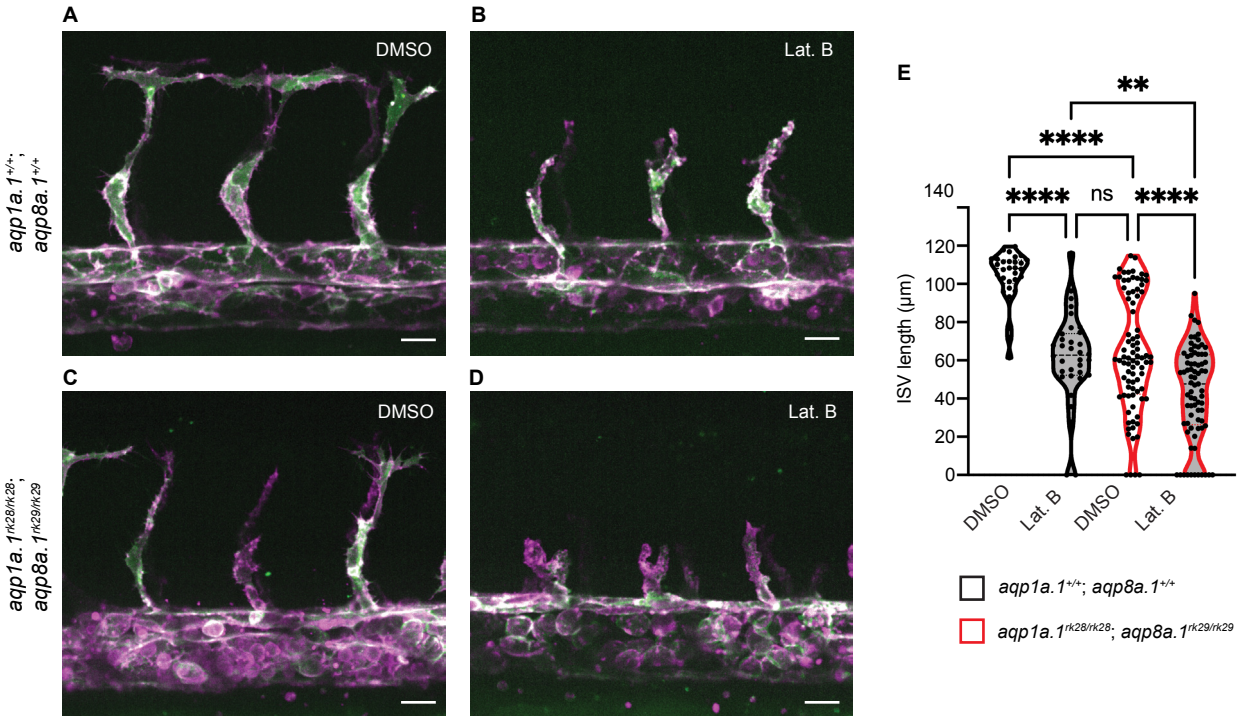

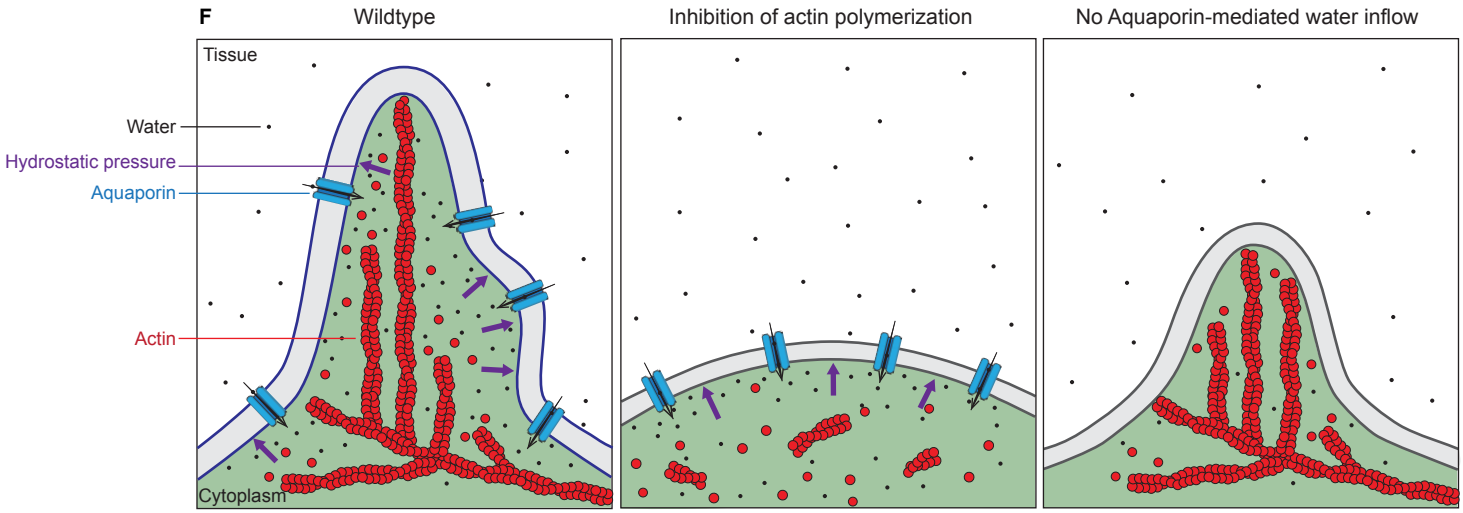

Membrane protrusion generated by actin polymerization and increased hydrostatic pressure.

Membrane protrusion generated by increased hydrostatic pressure.

Membrane protrusion generated by actin polymerization.